https://doi.org/10.5194/egusphere-2024-1425
Preprint. Discussion started: 18 June 2024

Freshwater input from glacier melt outside Greenland alters modeled northern high-latitude ocean circulation

Jan-Hendrik Malles[1,2], Ben Marzeion[1,2], and Paul G. Myers[3]

[1]Institute of Geography, University of Bremen, Bremen, Germany
[2]MARUM - Center for Marine Environmental Sciences, University of Bremen, Bremen, Germany
[3]Department of Earth and Atmospheric Sciences, University of Alberta, Edmonton, Canada

Correspondence: Jan-Hendrik Malles (jmalles@uni-bremen.de)

Abstract. As anthropogenic climate change depletes Earth's ice reservoirs, large amounts of freshwater are released into the ocean. Since the ocean has a major influence on Earth's climate, understanding how the ocean changes in response to an increased freshwater input is crucial for understanding ongoing shifts in the climate system. Moreover, to comprehend the evolution of ice-ocean interactions, it is important to investigate if and how changes in the ocean might affect marine-terminating glaciers' stability. Though most attention in this context has been on freshwater input from Greenland, the other northern hemisphere glacierized regions are losing ice mass at a combined rate roughly half that of Greenland, and should not be neglected. In order to get a first estimate of how glacier mass loss around the Arctic affects the ocean and how potential changes in the ocean circulation might affect marine-terminating glaciers, we conduct one-way coupled experiments with an ocean general circulation model (NEMO-ANHA4) and a glacier evolution model (Open Global Glacier Model; OGGM) for the years 2010 to 2019. We find an increase in heat content of Baffin Bay and changes in the subpolar gyre's structure. Additionally, we find a decreased heat transport into the Barents Sea due to increased freshwater input from Svalbard and the Russian Arctic. The rerouting of Atlantic water from the Barents Sea Opening through Fram Strait leads to an increased heat transport into the Arctic Ocean and a decrease of sea ice thickness in the Fram Strait area.

1 Introduction

The recent accumulation of heat in Earth's atmosphere and ocean due to anthropogenic climate change is diminishing the frozen water reservoirs on the planet, causing the release of large amounts of freshwater (Slater et al., 2021). Melting of Earth's glaciers is impacting regional hydrology and increasing global mean sea-level (GMSL; Huss and Hock, 2018; Frederikse et al., 2020). Moreover, such an additional freshwater input to the ocean changes its surface density and thus has the potential to change the ocean circulation on scales ranging from individual fjords (Bartholomaus et al., 2016) to the Atlantic Meridional Overturning Circulation (AMOC; Hu et al., 2011; Frajka-Williams et al., 2016), which is an important component of the global climate system. While there have been numerous studies on changes in the AMOC's strength and a potential influence of recently increased freshwater influx and ocean warming, it is disputed whether the AMOC has already been forced out of its natural variability envelope (Jackson et al., 2022; Latif et al., 2022; Caesar et al., 2021; Fu et al., 2020; Böning et al., 2016). Concerning the regional impact of enhanced Greenland ice sheet (GrIS) freshwater runoff on ocean circulation, Castro

https://doi.org/10.5194/egusphere-2024-1425
Preprint. Discussion started: 18 June 2024

de la Guardia et al. (2015) found significant changes in Baffin Bay in a numerical ocean circulation model. These changes entailed an increasing heat content in Baffin Bay with increasing (idealized) freshwater input along Greenland's west coast. This is a potential positive feedback, which could lead to larger heat transports towards marine-terminating glacier fronts. Anthropogenic climate change causes the ocean to take up vast amounts of heat (von Schuckmann et al., 2020). This increase in ocean temperature, in combination with potential changes in ocean circulation, increases submarine melt of marine-terminating glaciers, destabilizing their fronts and inducing further retreat and mass loss (Wood et al., 2021, 2018). Such interactions between changes in ice bodies and the ocean do not only bear importance for contemporary changes in the Earth system, but on time scales encompassing glacial cycles as well (Alvarez-Solas et al., 2013; Rainsley et al., 2018). This underscores the importance of knowledge about the coupled ice-ocean system for understanding past and ongoing changes of the Earth system, and for projecting future changes. While there has been previous research on the impact of Greenland melt on modeled ocean properties and the AMOC, they have either added an idealized high ('worst-case scenario') freshwater flux from Greenland only (e.g., Weijer et al., 2012; Castro de la Guardia et al., 2015), or did not disentangle the impact of the freshwater flux from Greenland and from the glaciers in regions surrounding it (e.g., Devilliers et al., 2021).

Although most attention in the context of ice-ocean interactions has been on the GrIS, as it is the largest land-ice reservoir in the northern hemisphere, there are also other places experiencing glacier mass loss and hence are releasing freshwater into the ocean. Around the high-latitude (North Atlantic and Arctic) ocean, such places are the Canadian Arctic Archipelago, Svalbard, Iceland, and the Russian Arctic. Since ice loss in these places combined is roughly half that of the GrIS (Hugonnet et al., 2021; Zemp et al., 2019; Slater et al., 2021), it is worth investigating whether increased freshwater input at the coasts of the aforementioned regions does affect the high-latitude ocean's circulation, as such changes might also impact marine ecosystems (Timmermans and Marshall, 2020; Hátún et al., 2009; Wassmann et al., 2011; Greene et al., 2008). Figure 1 charts the main features of the ocean surface currents in the Northern Atlantic and the gateways between the Atlantic and Arctic Ocean. Atlantic water masses (red) are characterized as warmer and more saline compared to the Arctic water (blue). Atlantic water is transported to the north, via the North Atlantic Current, by a complex interplay of the mainly wind-driven subtropical and subpolar gyres and the density-driven AMOC. The subpolar gyre (SPG) is the circulation pattern around the Labrador Sea and the Irminger Sea, which transports Atlantic water branching off to the west in the Irminger Sea to the Labrador Sea, and into Baffin Bay via the West Greenland Current. The Labrador Sea also is a location of importance for the AMOC, as deep convection takes place there (Broecker, 1997; Yeager et al., 2021), although this view was recently challenged (Lozier et al., 2019). Warm Atlantic water mainly enters the Arctic Ocean through Fram Strait as well as through the Barents Sea, while Arctic water mainly enters the Atlantic Ocean through the Canadian Arctic Archipelago (CAA) and Fram Strait (Lien et al., 2013; Myers et al., 2021; Rudels et al., 2005). Arctic water is transported further to the south mainly by the Labrador Current.

The amount of ice that is removed from glaciers (outside the GrIS) by submarine melt is essentially unknown. Submarine melt remains elusive, since it is intricate to measure directly and observations hence remain sparse. Attempts to quantify it therefore mostly rely on high-resolution ($\sim$1 m grid spacing close to the ice front) ocean circulation models and employing a parameterization of ice-ocean heat transfer related to oceanic properties at the glacier front (Jenkins et al., 2001; Holland et al., 2008; Xu et al., 2013). As this is computationally costly and can only be applied to individual glaciers, a further step in

https://doi.org/10.5194/egusphere-2024-1425
Preprint. Discussion started: 18 June 2024

trying to generalize such modeling results to different glaciers was to employ empirical power laws to describe the relationship between submarine melt and ocean properties as well as subglacial discharge (Xu et al., 2013; Rignot et al., 2016; Wood et al., 2021). We make use of such a power law parameterization in our attempt to quantify submarine melt of marine-terminating glaciers outside the GrIS.

To tackle the issue of ice-ocean interactions outside the GrIS, we one-way couple the Nucleus for European Modelling of the Ocean (NEMO) model and the Open Global Glacier Model (OGGM) for the years 2010 - 2019. We run both models twice, in order to investigate potential coupling effects. In one NEMO experiment, we use glacial surface mass loss and frontal ablation derived from OGGM as additional liquid freshwater and iceberg input to NEMO, while we omit this additional freshwater forcing in the second NEMO run. Next, we use the two different NEMO runs' output variables as forcing of the submarine melt parameterization newly implemented in OGGM (see section 2.5.1). We then explore the differences in results obtained from the two different NEMO and OGGM experiments to obtain a first-order estimate of the magnitude of the effect the ice-ocean coupling outside Greenland has on ocean properties as well as on marine-terminating glacier mass loss. Finally, we discuss future avenues for research on this topic, as our rather simple approach warrants further work on more closely examining the mechanisms proposed in this work.

https://doi.org/10.5194/egusphere-2024-1425
Preprint. Discussion started: 18 June 2024

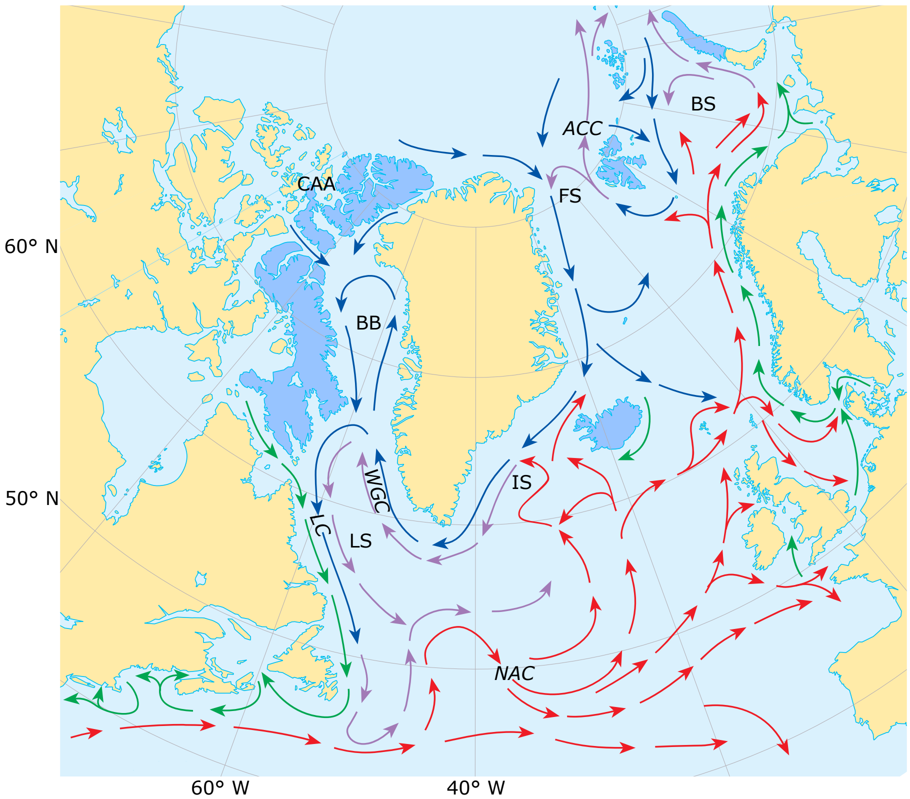

Figure 1. Schematic of the main surface currents in the North Atlantic Ocean. Red/blue arrows indicate Atlantic/Arctic water, and purple arrows a mixture of both water masses. Green arrows indicate coastal water masses. Blue colored land areas indicate regions that contain glaciers outside of Greenland, see Figs. 12 and A2 for the actual glacier outlines. Italic acronyms represent ocean current names, while the others represent location names.

https://doi.org/10.5194/egusphere-2024-1425
Preprint. Discussion started: 18 June 2024

2 Data and Methods

2.1 Ocean model

Our numerical experiments were conducted with NEMO v3.6 (Madec et al., 2016), which is coupled to a sea ice model (Louvain-la-Neuve Sea Ice Model 2; Bouillon et al., 2009). The configuration we use covers the Arctic and Northern Hemisphere Atlantic and has open boundaries at 20°S in the Atlantic Ocean as well as at the Bering Strait. The average horizontal resolution of the model is 1/4°, and it has 50 vertical levels (Arctic and Northern Hemisphere Atlantic (ANHA4) configuration; see Fig. A1). For boundary and initial ocean conditions we use the Global Ocean ReanalYsis and Simulations data (GLORYS2v3; Masina et al., 2017) and for atmospheric forcing the Canadian Meteorological Center's reforecasts (CGRF; Smith et al., 2014). CGRF provides hourly fields of wind, air temperature and humidity, radiation fluxes, and total precipitation with a horizontal resolution of 33 km, which are linearly interpolated onto the NEMO-ANHA4 grid. The Lagrangian iceberg module implemented in NEMO is described by Marsh et al. (2015) and was further developed by Marson et al. (2018). The baseline continental runoff data (outside Greenland) for our runs was obtained by linearly interpolating the data provided by Dai et al. (2009) on a $1 \times 1°$ grid to the NEMO-ANHA4 grid. The Dai et al. (2009) data do not cover our model period from 2010 to 2019. We therefore applied the 1997 to 2007 monthly average baseline runoff. Freshwater input from Greenland is derived by remapping the data published by Bamber et al. (2018) to the NEMO-ANHA4 grid. This data gives the total runoff, including from the ice sheet and peripheral glaciers, thus replacing the baseline runoff in this region. As this data set only ranges to the end of 2016, we use the 2010 to 2016 average for the three missing years. Runoff freshwater is added to the first vertical model level with a temperature corresponding to the surface temperature of the ocean grid cell, for the lack of a more accurate temperature estimate. The addition of runoff entails an increase in the vertical mixing (diffusivity) parameter for the grid cell's upper 30 m in our setup (from the background value of 1×10^{-5} to 2×10^{-3} m^2 s^{-1}), following Marson et al. (2021). Bamber et al. (2018) give data for liquid runoff and solid ice discharge around Greenland. Here, we add half of the solid discharge estimates to the liquid freshwater input and the other half to the iceberg module, following the observation by Enderlin et al. (2016) that roughly half of the icebergs' volume may melt before they exit fjords. The handling of additional freshwater from other glacierized regions is described in section 2.4. Apart from our newly added freshwater flux, NEMO-ANHA4 setups akin to the one described here have been used before to study ocean circulation processes in the northern high-latitudes (Castro de la Guardia et al., 2015; Garcia-Quintana et al., 2019; Gillard et al., 2022; Pennelly and Myers, 2021).

2.2 Glacier model

The Open Global Glacier Model (OGGM) is a flowline model that can be used to model a large number of individual glaciers at once (Maussion et al., 2019). Because observational data on glaciers, needed to constrain more complex representations of glaciological processes (e.g., ice thickness, spatial distribution of mass balance, albedo, basal velocity) are scarce, its computational cost is relatively low. We use the Randolph Glacier Inventory (RGI) version 6 (RGI Consortium, 2017; Pfeffer et al., 2014) to initialize the model for the ∼15,000 glaciers surrounding the Arctic and North Atlantic (outside the GrIS) that are included in our study. Topographical data is obtained from an appropriate digital elevation model (DEM), depending on the

https://doi.org/10.5194/egusphere-2024-1425
Preprint. Discussion started: 18 June 2024

glacier's location (details in Maussion et al. (2019)). Here, we use single, binned elevation-band flowlines, constructed from the outlines and topographical data, using the approach described by Werder et al. (2020). Simulations of OGGM start in the year the glacier outlines contained in the RGI were recorded. The gridded atmospheric forcing data (monthly temperature and precipitation obtained from Climatic Research Unit Time-Series data set version 4.03 (CRU TS 4.03, Harris et al., 2020)) are interpolated to the glacier location. Temperatures are subsequently adjusted applying a linear lapse rate (6.50 °C/km) that is fixed globally. For precipitation, no lapse rate, but a global correction factor is applied (here, we use a value of 2.5), which is a common approach in large-scale glacier modeling (e.g., Giesen and Oerlemans, 2012; Zekollari et al., 2022). The resulting temperature and precipitation values are used to compute the glaciers' surface mass balance by using a temperature-index melt model, which calculates surface melt rates from the near-surface atmospheric temperatures above a threshold temperature and neglects more intricate processes such as refreezing and the surface energy balance. The melt factor is calibrated using satellite-derived observations of glacier mass changes (Hugonnet et al., 2021). For an elaborate description of OGGM, the reader is referred to Maussion et al. (2019).

Modeling marine-terminating glaciers requires some additional model features compared to land-terminating ones. That is because additional processes occur at their fronts which determine their dynamical behavior. The two main processes are an increasing basal/sliding velocity, moderated by the hydrostatic stress balance close to the front, and frontal ablation. Therefore, water-depth dependent sliding, hydrostatic stress coupling, and frontal ablation parameterizations were incorporated into OGGM's ice thickness inversion as well as ice dynamics schemes. To be able to calibrate the surface and frontal ablation parameterizations separately, the two mass budget parts have to be disentangled from observational data. For this purpose, the frontal ablation data of Kochtitzky et al. (2022) is used in addition to the data of Hugonnet et al. (2021). Frontal ablation is parameterized by using a linear scaling to the water depth:

$$Q_{fa} = k d_f h_f w_f \tag{1}$$

where Q_{fa} is the frontal ablation flux (in m^3 a^{-1}), k the frontal ablation parameter (in a^{-1}), and d_f, h_f, and w_f the water depth, ice thickness, and ice width at the glacier front. In order to simulate submarine melt in OGGM, another parameterization is introduced, which will be described in section 2.5.1. More details of marine-terminating glacier modeling in OGGM are given in Malles et al. (2023).

2.3 One-way coupling of NEMO and OGGM

In order to estimate the effects of freshwater input to NEMO that is usually not accounted for, as well as the amount of mass removal from marine-terminating glaciers (outside the GrIS) by submarine melt, we adopt a simple one-way coupling scheme. This means we do not update the input to one model derived from the other one during the simulations. However, we implement the one-way coupling in both directions separately, so that we can roughly estimate the strength of any potential feedback. In the following, we describe how the respective inputs were derived and used for both models.

https://doi.org/10.5194/egusphere-2024-1425
Preprint. Discussion started: 18 June 2024

2.4 OGGM to NEMO

In one of our NEMO experiments, we use the OGGM output of glaciers' surface mass loss in addition to half of the frontal ablation as additional liquid freshwater forcing, while the other half of the frontal ablation is added to the iceberg module, as is done for the Greenland solid ice discharge (this experiment hereafter is named *halfsolid*). We neglect the OGGM-freshwater and -iceberg fluxes in the other NEMO experiment (hereafter called *noOGGM*). Note that the liquid freshwater and iceberg input around Greenland is derived from Bamber et al. (2018). This data set contains total runoff and solid ice discharge, including from peripheral glaciers, and is the same in both NEMO runs. The distribution of the resulting liquid freshwater forcing (excluding the baseline runoff described in the previous section) is displayed in Fig. A2. The liquid freshwater input (excluding the baseline runoff), averaged over 2010 to 2019, amounts to approximately 32 mSv ($\approx$ 1011 Gt a^{-1}) in the *halfsolid* run and of approximately 29 mSv ($\approx$ 903 Gt a^{-1}) in the *noOGGM* run. The calving input distribution is displayed in Fig. A3, which amounts to an average of approximately 9 mSv ($\approx$ 276 Gt a^{-1}) in the *halfsolid* run and to approximately 8 mSv ($\approx$ 248 Gt a^{-1}) in the *noOGGM* run. This means that OGGM contributes roughly 4 mSv additional freshwater in the *halfsolid* run; approximately half the freshwater amount released to the ocean due to GrIS mass loss. The liquid freshwater from surface melt and the calving of individual glaciers deducted from OGGM output are put into the NEMO-ANHA4 grid cell with the lowest haversine distance to the respective glacier terminus location recorded in the RGI.

2.5 NEMO to OGGM

We use the outputs of the two NEMO experiments described above to calculate the thermal forcing of the ocean in the vicinity of marine-terminating glacier termini, which is then fed to the submarine melt parameterization of OGGM described below. Thermal forcing is defined as the (positive) difference between the potential temperature of a water mass and its freezing point. Here, we use the pressure- and salinity-dependent formulation of the freezing point given in Fofonoff and Millard Jr (1983).

2.5.1 Submarine melt parameterization in OGGM

While there has been previous work on incorporating frontal ablation into OGGM (Malles et al., 2023), it did not yet explicitly account for submarine melt. In this work we build on the previous work and add a parameterization of submarine melt rates (in m d^{-1}) following Rignot et al. (2016):

$$q_{sm} = (Ad\, q_{sg}^{\alpha} + B)\, T_f^{\beta} \tag{2}$$

where A is the subglacial discharge scaling parameter (in d$^{\alpha-1}$ m$^{-\alpha}$ K$^{-\beta}$), d the water depth at the glacier front (in m), q_{sg} the subglacial discharge normalized by submerged cross-section area at the glacier terminus (in m d^{-1}), α the subglacial discharge scaling exponent (dimensionless), B the ocean heat transfer scaling parameter (in m d^{-1} K$^{-\beta}$), T_f the oceanic thermal forcing in the vicinity of the glacier terminus (in K), and β the ocean heat transfer scaling exponent (dimensionless).

https://doi.org/10.5194/egusphere-2024-1425
Preprint. Discussion started: 18 June 2024

Equation 2 comprises two nested empirical power laws relating subglacial discharge and ocean potential temperature as well as salinity to submarine melt rates. The first power law (first term in the brackets) describes the increase in thermal erosion of marine-terminating glacier fronts due to subglacial discharge (q_{sg}). It is based on a statistical fit to modeling results that applied a parameterization, which was developed to represent heat and freshwater exchange across the ice-ocean interface in relation to ice temperature and ocean properties (Jenkins et al., 2001). This approach to computing freezing and melting at an ice-ocean interface, in combination with the injection of subglacial discharge, was used to model the circulation in front of a vertical ice cliff in a high-resolution ocean model and the resulting submarine melt (Xu et al., 2013). In essence, this power law expresses the increase in turbulence close to the glacier front in the presence of subglacial discharge, which increases the entrainment of warmer and saltier water from the ocean into the buoyant plume of freshwater. Suitable values for the exponent α were found to be below 1, since there is a saturation of the melt intensity caused by subglacial discharge. This is because the plume-ice contact area can no longer significantly increase at some point (Slater et al., 2016), while increasing subglacial discharge causes a freshening, and thus lower thermal forcing, of the water close to the glacier terminus. Values for the scaling parameter (A) are related to the vertical temperature gradient in front of the glacier and to the distribution and morphology of the subglacial discharge plumes along the glacier front. The second power law (BT_f^{β}) parameterizes the heat transport from the ocean to the ice and the resulting submarine melt in the absence of subglacial discharge. The scaling parameter B relates to the open ocean and fjord currents as well as to the ice temperature. The exponent β is related to the nonlinear relationship between submarine melt and thermal forcing (T_f) found by Xu et al. (2013) and Holland et al. (2008), which is based on the idea that submarine melt supplies buoyancy forcing to the plume convection at the glacier front, thereby increasing the entrainment of the open ocean's thermal forcing. Generally, the presence of icebergs in a fjord can change the fjords' water properties and thereby have an impact on submarine melt as well (Kajanto et al., 2023; Moon et al., 2018; Davison et al., 2020), but we neglect this here for simplicity.

To calculate total frontal ablation rates and to emulate calving due to the undercutting of glacier fronts by submarine melt, we adapt the parameterization of total frontal ablation rates previously applied in OGGM (see Eq. 1) to:

$$q_{fa} = max(kd, q_{sm}\frac{h}{d}) \tag{3}$$

where k (in a^{-1}) is the frontal ablation parameter, and h the ice thickness at the glacier front (in m). This allows for applying the values of the glacier-specific frontal ablation parameters that were calibrated by Malles et al. (2023), while constraining the parameters involved in the submarine melt parameterization as well, by ensuring that the total frontal ablation over the modeling period lies within the observationally estimated range given by Kochtitzky et al. (2022). As there are little to no observational estimates of submarine melt itself, it is not possible to constrain the four free parameters in Eq. 2 (A, α, B, β) for each glacier individually. Even if we had such estimates, we might be able to find different parameter combinations that complied with such observations. While this submarine melt parameterization has some physical foundations and was already applied in previously published works, it overparameterizes the model, because it introduces four additional parameters without additional observations to calibrate these. Therefore, we apply latin hypercube sampling to identify parameter sets that are

https://doi.org/10.5194/egusphere-2024-1425
Preprint. Discussion started: 18 June 2024

consistent with observations of total frontal ablation over the same time period as the OGGM run (2010 to 2019). The latin hypercube sampling technique can generally provide a better coverage of the parameter space than random sampling (McKay et al., 1979) and is thus appropriate in our use case, since we know the bounds of the parameter space to be sampled only roughly. To balance computational cost and coverage of the parameter space, we sampled the following intervals 25 times:

- A: [3 x 10^{-5}, 1 x 10^{-3}]
- α: [0.25, 0.7]
- B: [1 x 10^{-3}, 0.75]
- β: [1.0, 2.0]

We run OGGM with each of the 25 sampled parameter sets for each marine-terminating glacier utilizing the halfsolid run output's thermal forcing. Afterwards, we only pick results from the parameter sets that yield total frontal ablation rates within the uncertainty bound of the observational estimates by Kochtitzky et al. (2022). To investigate a potential coupling effect, we apply the parameter sets selected for the halfsolid run to the thermal forcing derived from the *noOGGM* NEMO run output in a subsequent OGGM simulation. For six glaciers we do not find any valid parameter combination, but these glaciers together make up less than 1 % of the total marine-terminating glacier volume.

Thermal forcing values from the ocean model output are obtained by taking all NEMO-ANHA4 grid cells within a 50 km radius of the respective marine-terminating glacier's terminus into account. If there are less than 3 ocean model grid cells in the radius, we iteratively double the radius. This ensures that we do not only use the value from a single ocean model grid cell, since we do not know whether the closest one actually reflects water properties at the glacier front best. We then compute a depth-averaged value of the included cells' thermal forcing and apply a distance-weighted averaging to obtain the final value inserted in Equation 2. Here we use the full depth range of the grid cells, as NEMO-ANHA4 does not resolve individual fjords and it is unclear which depth range of the open ocean would be appropriate to include.

3 Results

3.1 Ocean model

In this section we will describe our findings regarding differences between the *halfsolid* and the *noOGGM* runs (i.e., *halfsolid* minus *noOGGM*). Spatial plots display differences averaged over the last five years of the NEMO integrations (i.e., 2015 to 2019), assuming the initial upper ocean transient behavior has abated sufficiently during the first half of the simulations (Castro de la Guardia et al., 2015; Brunnabend et al., 2012), allowing us to explore the impact of the increased freshwater forcing in the halfsolid run. Potential impacts of the spin-up on our results will be discussed in more detail in section 4. Throughout this work we refer to the two main water masses of interest in a general manner: we use the term Atlantic for water moving from the Atlantic towards the Arctic Ocean, and the term Arctic for water moving in the opposite direction; implying that the former is

https://doi.org/10.5194/egusphere-2024-1425
Preprint. Discussion started: 18 June 2024

warmer and more saline than the latter. We abstain from distinguishing the water masses further by temperature and/or salinity criteria, as we are mostly interested in a first overview of total changes in ocean properties that might be relevant to ice-ocean coupling. Thus, the benefit of thoroughly segregating water masses is not apparent. Especially, since there are several water masses present in the Atlantic Ocean (Liu and Tanhua, 2021), and it is hence not clear which definition should be used for a general overview, though this could be examined in subsequent work focusing more in-depth on certain processes. In the following sections we will focus on the depth ranges 0-200 m, and 200-600 m, since most changes occur in these ranges and are relevant to potential feedbacks with marine-terminating glacier mass loss induced by submarine melt.

3.1.1 Baffin Bay and Canadian Arctic Archipelago

Figure 2 shows the differences in temperature averaged over the upper 200 m between the *halfsolid* and *noOGGM* run. An average warming of around 0.1 K in central and western Baffin Bay is visible. Towards the western coast the warming transitions to a slight cooling, due to the increased freshwater input at surface temperature. It might also play a role that in our model setup, the vertical mixing coefficient is increased for the upper 30 m (see section 2.1), which might expose more water to the cold atmosphere leading to enhanced vertical heat loss. Looking at the depth range of 200-600 m, a similar pattern is visible (Fig. A4), though without the cooling effect of increased freshwater input along the western coast. Since changes in heat content in Baffin Bay are caused by changes in lateral (advective) or vertical heat fluxes, there are three main mechanisms that might cause this warming: i) increased northward heat transport through Davis Strait, ii) less net volume transport from the Arctic through the Canadian Arctic Archipelago (i.e., Nares Strait, Lancaster Sound, and Jones Sound; hereafter named CAA), which leads to less lateral heat loss, and iii) stronger stratification leading to less vertical mixing and thus less heat transfer from the warmer subsurface water to the atmosphere. These mechanisms were previously investigated by Castro de la Guardia et al. (2015) in a study that conducted idealized NEMO experiments to investigate the effects of increased freshwater input along Greenland's (west) coast on Baffin Bay. Although Castro de la Guardia et al. (2015) increased the freshwater input at the east coast of Baffin Bay in their experiments, we observe some similar effects on the ocean properties in the Baffin Bay area in our simulations, where the main addition of freshwater is at the west coast of Baffin Bay. We find an increase in sea surface height (SSH) gradient from the eastern and western shelves of Baffin Bay towards its center, even though the increase in the eastern part is roughly one order of magnitude smaller than the one found by Castro de la Guardia et al. (2015). This leads to a stronger cyclonic circulation in Baffin Bay (see Figs. 3 and A5), which in turn leads to enhanced vertical velocities due to Ekman pumping, moving warmer subsurface waters from the WGC to shallower depths.

We also find an increase in northward (positive) volume transport through Davis Strait throughout our simulation period in the *halfsolid* run compared to the *noOGGM* run (approx. 0.05 Sv $\approx$ 3 %), which is balanced by an increasing southward (negative) outflow, along the cyclonic pattern of the Baffin Bay Gyre (see Fig. 4). The increase in northward volume flow is not caused by an increase in northward freshwater flux, since the amount of freshwater added to the Greenland coast south of Davis Strait does not differ between our two setups. Moreover, the average increase in northward heat transport we find in the second half of our simulations is approx. 1.1 TW, which is roughly 5 % of the average total northward heat transport. The increase in northward heat inflow we find comparing the first to the second half of our model integrations nearly quadruples

https://doi.org/10.5194/egusphere-2024-1425
Preprint. Discussion started: 18 June 2024

from ~0.25 TW, while the northward volume flux only doubles (see Fig. 4). This increase of the heat to volume transport ratio is likely associated with an increase in the WGC's strength and thus larger transport of warm Atlantic water into Baffin Bay (see. Fig. A6).

Across the CAA we observe the following changes: an increase in temperatures due to the enhanced northward heat transport from Baffin Bay, and a decrease in salinity due to increased freshwater input (see Figs. 5 and A7). The increase in temperature is more pronounced in the 200-600 m layer than in the 0-200 m depth range (see Fig. A8), as the increased freshwater input attenuates the enhanced heat import closer to the surface and the Atlantic water is typically situated more in the 200-600 m depth range. Particularly in areas close to Ellesmere Island's north coast the increased input of freshwater at the (cold) surface temperatures offsets the import of warmer waters from Baffin Bay in the 0-200 m depth range, resulting in slightly negative potential temperature differences (~ -0.03 K). Again, the vertical mixing coefficient might play a role here as well.

Concerning volume fluxes through the individual CAA straits considered here, the only statistically significant change we find in the second half of our simulations, is a positive shift in volume flux (~0.02 Sv) through Lancaster Sound. This amounts to ~3 % of the 0.6 Sv total southward (negative) flux (see Fig. A9) into Baffin Bay through this channel. There also is a small (0.014 Sv ≈ 0.8 %) decrease in overall volume flux through the CAA straits into Baffin Bay.

https://doi.org/10.5194/egusphere-2024-1425
Preprint. Discussion started: 18 June 2024

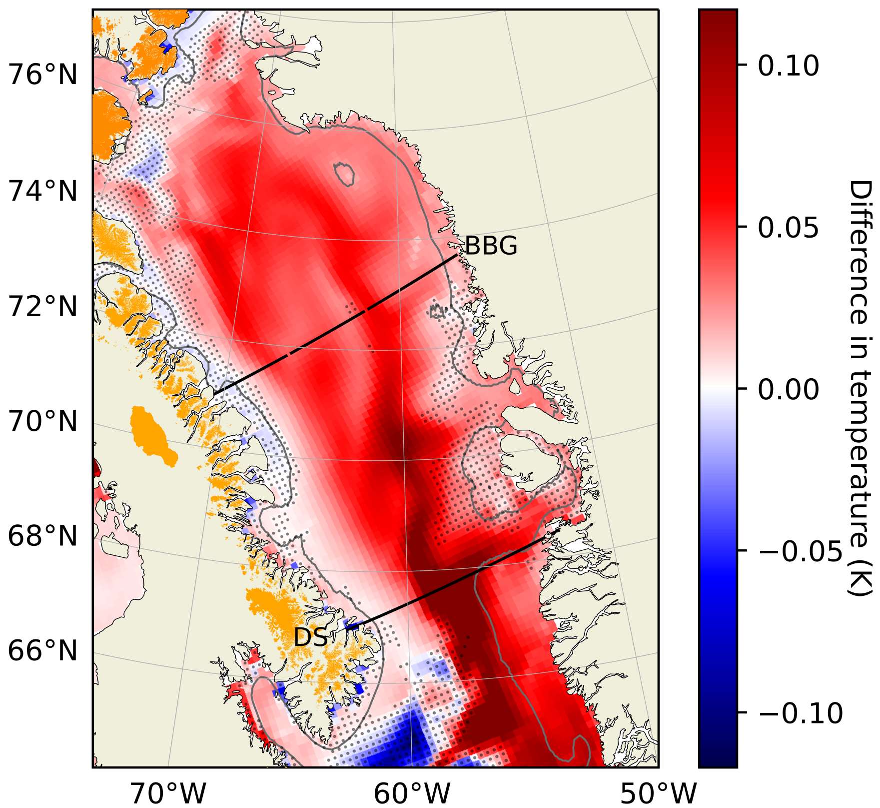

Figure 2. Difference in potential temperature averaged over up to 200 m water depth between the *halfsolid* and the *noOGGM* NEMO runs in Baffin Bay. Dots indicate differences that are not statistically significant, according to Wilcoxon signed-rank tests ($p > 0.05$). BBG stands for the Baffin Bay Gyre section and DS for the Davis strait section. Colored land area indicates glacierized area as recorded in the RGI. Grey lines show the low-pass filtered 200-m bathymetry contours.

https://doi.org/10.5194/egusphere-2024-1425
Preprint. Discussion started: 18 June 2024

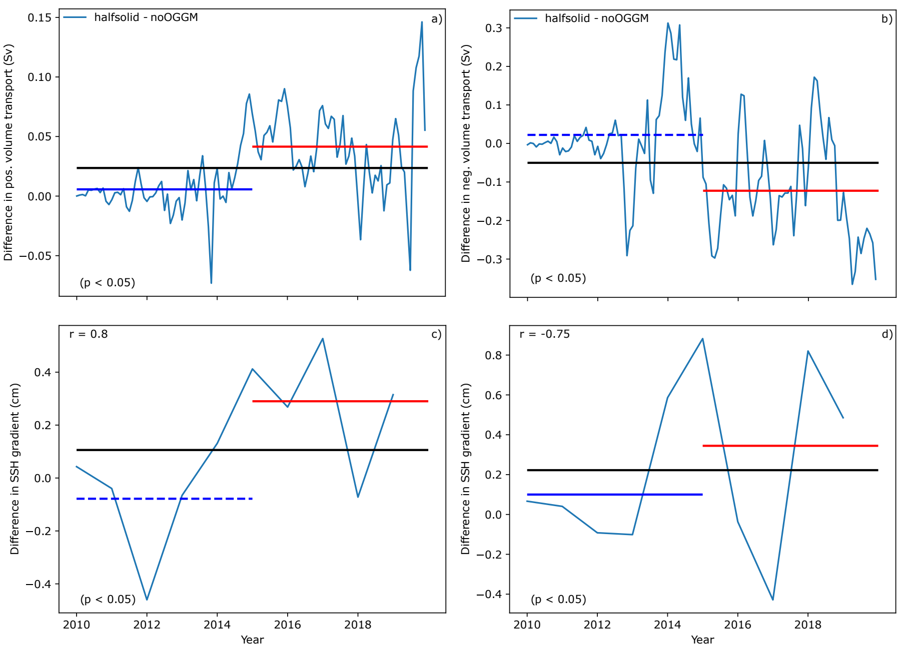

Figure 3. Differences in gyre strength and SSH gradients in Baffin Bay between the *halfsolid* and the *noOGGM* NEMO runs. a): northward (positive) volume transport through eastern part of the Baffin Bay Gyre (BBG) section in Fig. 2, b): southward (negative) volume transport through western part of the BBG section in Fig. 2, c): annual mean SSH gradient between point with the highest average SSH in the eastern part of the BBG section and the point with the lowest average SSH in the center part of the section, d): same as c), but for the point with the highest average SSH in western part of the BBG section. Differences in SSH gradients are displayed as annual means for better visibility. The lines in panels a) and b) show average differences over the first (blue) and last (red) five years, as well as over all years (black) of the model integrations. Values in the upper left corners of panels c) and d) are the correlation coefficients between annual mean north-/southward volume flux and SSH gradients from the east/west to the center of the Baffin Bay Gyre. Differences between the two NEMO runs that are statistically significant, according to Wilcoxon signed-rank tests ($p < 0.05$), are drawn as solid lines and dashed otherwise. Values in the lower left corners show the p-values of Wilcoxon signed-rank tests of differences between the differences of the first and last five modeled years.

https://doi.org/10.5194/egusphere-2024-1425
Preprint. Discussion started: 18 June 2024

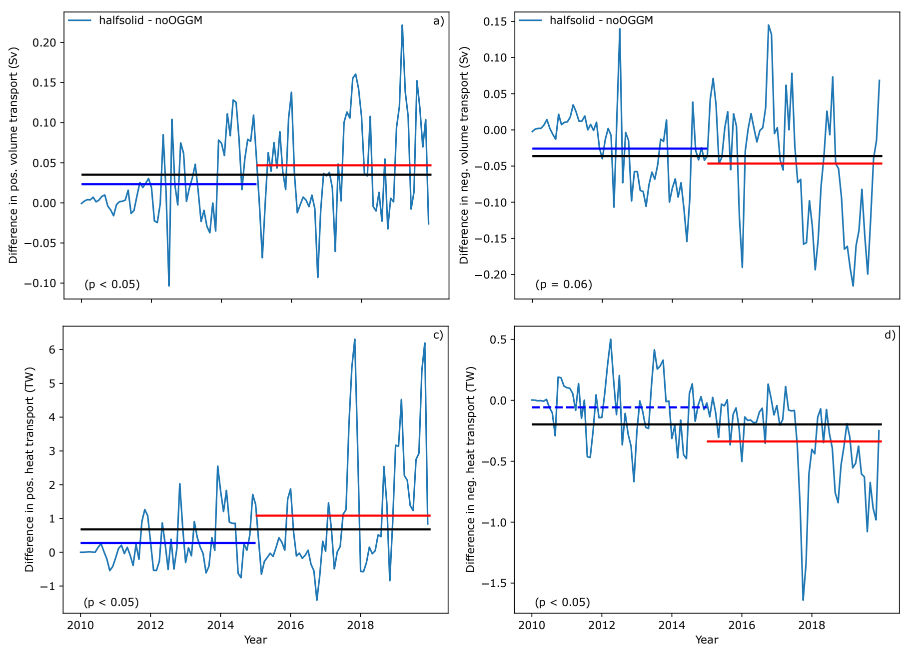

Figure 4. Differences in north- and southward volume and heat transport through Davis Strait between the *halfsolid* and the *noOGGM* NEMO runs. a): northward (positive) volume transport through Davis Strait (DS) section in Fig. 2, b): southward (negative) volume transport through DS, c): northward heat transport through DS, d): southward heat transport through DS. The lines show average differences over the first (blue) and last (red) five years as well, as over all years (black) of the model integrations. Differences between the two NEMO runs that are statistically significant, according to Wilcoxon signed-rank tests ($p < 0.05$), are drawn as solid lines and dashed otherwise. Values in the lower left corners show the p-values of Wilcoxon signed-rank tests of differences between the differences of the first and last five modeled years.

https://doi.org/10.5194/egusphere-2024-1425
Preprint. Discussion started: 18 June 2024

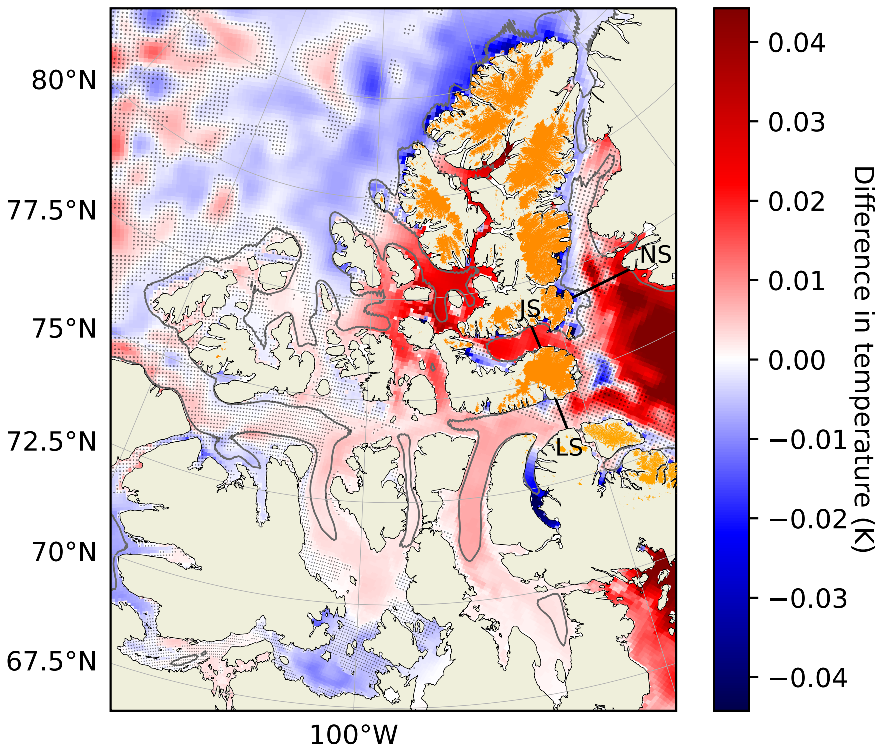

Figure 5. Difference in potential temperature averaged over up to 200 m water depth between the *halfsolid* and the *noOGGM* NEMO runs in the CAA region. NS stands for the Nares Strait, JS for the Jones Sound, and LS for the Lancasters sound section. Dots indicate differences that are not statistically significant, according to Wilcoxon signed-rank testss ($p > 0.05$). Colored land area indicates glacierized area as recorded in the RGI. Grey lines show the low-pass filtered 200-m bathymetry contours.

https://doi.org/10.5194/egusphere-2024-1425
Preprint. Discussion started: 18 June 2024

3.1.2 Subpolar Gyre and AMOC

Figure 6 shows differences in mixed layer depth as well as in density, salinity, and temperature between our two NEMO runs over the upper 200 m in the area of the SPG. The differences in mixed layer depth in the Labrador Sea region between our two NEMO runs, while in part statistically significant, are within the model's as well as observed interannual variability (Kieke and Yashayaev, 2015). The differences in mixed layer depth are related to the differences in density, which show a varied pattern across the SPG. While in the northern part of the Labrador Sea density is increased, it is decreased in the central and southern Labrador Sea. This is caused by two competing mechanisms: i) increased import of (cold) freshwater due to the increased input upstream of the Labrador Current caused by glacial melt, and ii) increased entrainment of warm and saline water from the enhanced WGC. There is also more cold and fresh water accumulation in the eastern half of the SPG, resulting in a higher density there. These differences in density are, in turn, translated to differences in the SSH, which show an increase in the central and southern Labrador Sea, and a decrease in the northern Labrador Sea and the eastern SPG (see Fig. 7). Finally, the SSH changes induce changes in the geostrophic circulation, illustrated by the differences in the barotropic streamfunction (BSF; see Fig. 7). The BSF is increased in the central Labrador Sea, indicating an anticyclonic tendency, while it is slightly decreased in the eastern SPG, suggesting that the center of the gyre circulation shifts slightly in the *halfsolid* compared to the *noOGGM* simulation. Further, negative salinity differences in the western Labrador Sea in the 200-600 m depth range (see Fig. A10 panel c)) suggest an enhanced recirculation of Labrador Current water (Lavender et al., 2000). In this depth range the warming in the central Labrador Sea due to enhanced import of Atlantic water is more pronounced as well (see Fig. A10 panel d)). This partly offsets the freshening from the hypothesized recirculation in that depth range, leading to a weaker density decrease in the central Labrador Sea than in the 0-200 m range, while the enhanced recirculation attenuates the warming due to entrainment of WGC water into the northern Labrador Sea.

Concerning the AMOC, we neither find a statistically significant difference in north-/southward or total volume flux across the 47°N latitude in the Atlantic, nor a significant change in the meridional overturning streamfunction. This suggests that there are no significant differences in AMOC strength between the *halfsolid* and *noOGGM* experiment. Although we find significant changes in the Labrador Sea's and the SPG's properties, this does not affect the AMOC in a meaningful way. While there were contrasting findings concerning the Labrador Sea's role in affecting the AMOC in previous studies, the differences between our model runs might just not be large enough to have an effect on that large-scale circulation feature (Böning et al., 2016; Garcia-Quintana et al., 2019).

https://doi.org/10.5194/egusphere-2024-1425
Preprint. Discussion started: 18 June 2024

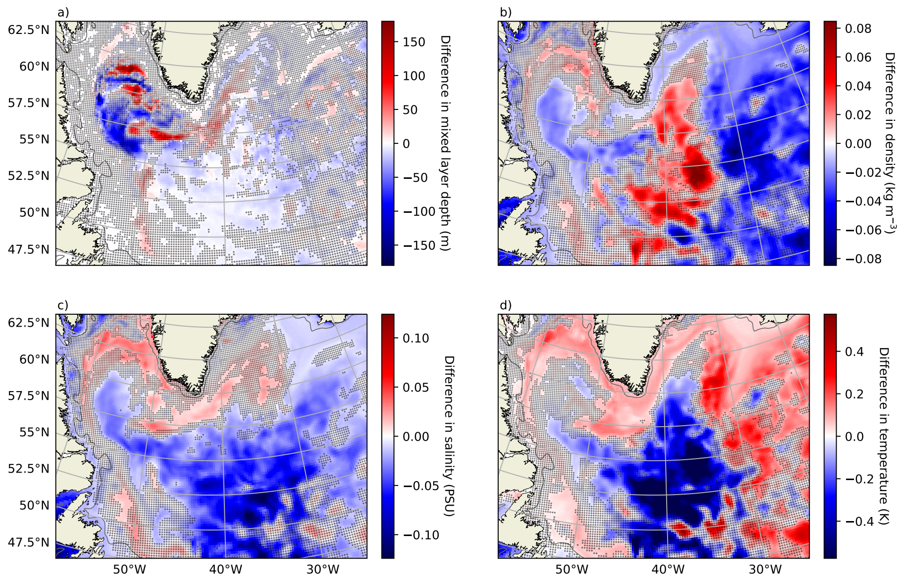

Figure 6. Difference in a) mixed layer depth, b) density, c) salinity, and d) potential temperature averaged over up to 200 m water depth between the *halfsolid* and the *noOGGM* NEMO runs in the supolar gyre region. Dots indicate differences that are not statistically significant, according to Wilcoxon signed-rank tests (p > 0.05). Grey lines show the low-pass filtered 200-m bathymetry contours.

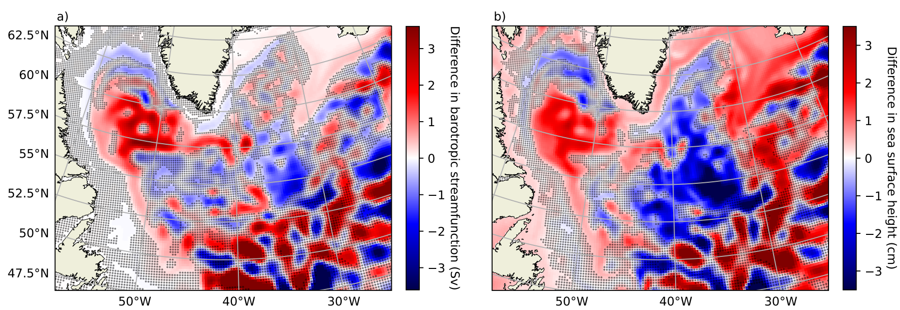

Figure 7. Difference in a) barotropic streamfunction, and b) sea surface height between the *halfsolid* and the *noOGGM* NEMO runs in the supolar gyre region. Dots indicate differences that are not statistically significant, according to Wilcoxon signed-rank tests (p > 0.05).

https://doi.org/10.5194/egusphere-2024-1425
Preprint. Discussion started: 18 June 2024

3.1.3 Barents and Nordic Seas

We show the SSH difference between the *halfsolid* and the *noOGGM* runs in Fig. 8. The increased freshwater input from Svalbard and the Russian Arctic in the *halfsolid* run (see Fig. A2) increases the SSH in the northern Barents Sea. This leads to an increased anticyclonic circulation around that area (see Fig. A11), leading, in turn, to a lower volume flux through the Barents Sea Opening. This is consistent with findings by Lien et al. (2013) and implies a lower (positive) flux of Atlantic water into the Barents Sea, decreasing temperatures in most parts (see Fig. 9 and Fig. 10 panel a)). The volume flux out of the Barents Sea increases, leading to a net volume flux decrease of 0.11 Sv (≈4 %). However, the flux of freshwater (using a reference salinity of 34.8 PSU) out of Barents Sea through the BSO decreases by 8 % (Fig. 10 panel c)), meaning that the additional freshwater input from Svalbard and the Russian Arctic partly remains in the Barents Sea and Arctic Ocean, and that the freshwater input leaving through the BSO is salinified. This also shows in the decreased salinity values in the western Barents Sea and in the Kara Sea (see Fig. A12).

The Atlantic water not entering the Barents Sea is routed towards the Fram Strait instead, leading to an increased northward (positive) volume flux (see Fig. 10 panel b)). Some of this warm water subsequently enters the Barents and Kara Seas from the north (see Fig. 9), contributing to the increased outflow through the BSO described above. The remainder of the Atlantic water rerouted through Fram Strait follows roughly the eastern Arctic shelf break (see next section). The increase in positive volume flux through Fram Strait begins after roughly half of the NEMO integration time, presumably due to the buildup of meltwater during that period leading to the increased BSF around Svalbard. This increase in volume flux into the Arctic Ocean through Fram Strait is accompanied by an increased outflux, yielding a net increase in northward (positive) volume flux through Fram Strait of ∼0.24 Sv (≈ 9 %). The increase in southward (negative) flux of freshwater through Fram Strait is small and statistically not significant, indicating that the enhanced southward flux is due to enhanced recirculation of Atlantic water. Since not all of the increased volume flux into the Arctic through Fram Strait can be explained by the net positive (eastward) volume flux difference we find for the Barents Sea, we also analyzed the volume fluxes through the Denmark Strait, finding a decrease in southward (negative) as well as an increase in northward (positive) transport, mainly in the 200-600 m depth range. The net increase of ∼0.1 Sv (≈ 3 %) through Denmark Strait almost closes the gap between the net decrease of Atlantic water volume flux into the Barents Sea and the net increase of the same into the Arctic Ocean through Fram Strait. We also find a small (0.07 Sv), although not statistically significant, increase of net northward volume flux between Iceland and Scotland. The changes in volume fluxes through Denmark Strait and between Iceland and Scotland could be linked to the changes in SSH in the areas of the Norwegian and Greenland Seas as well as around Iceland (see Figs. 8 and 7 a)), which, together with the BSF changes in Fig. A11, indicate an increased strength of the gyres present in these areas (Raj et al., 2019; Chatterjee et al., 2018).

https://doi.org/10.5194/egusphere-2024-1425
Preprint. Discussion started: 18 June 2024

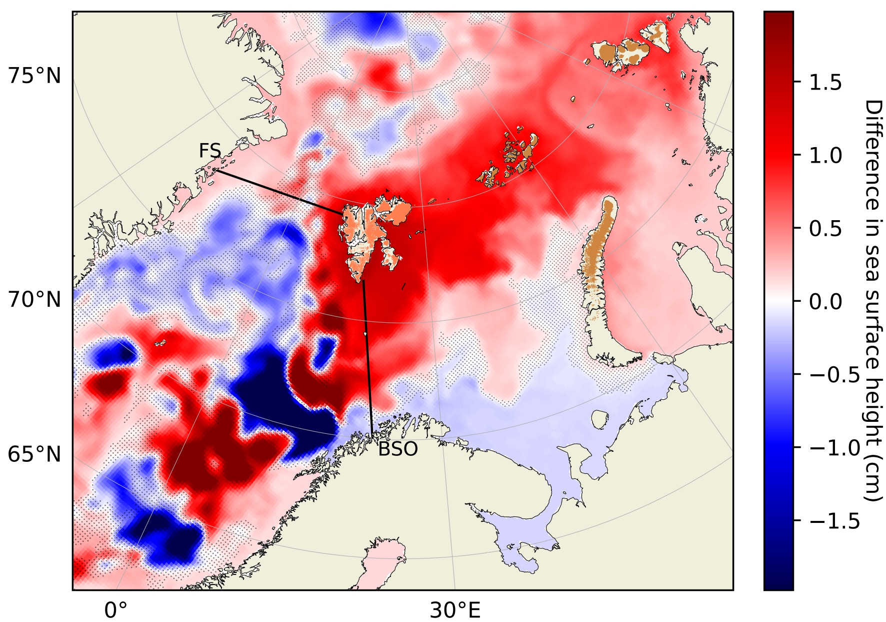

Figure 8. Difference in sea surface height between the *halfsolid* and the *noOGGM* NEMO runs in the Barents and Nordic Seas area. Dots indicate differences that are not statistically significant, according to Wilcoxon signed-rank tests ($p > 0.05$). FS stands for Fram Strait and BSO for Barents Sea Opening sections. Colored land area indicates glacierized area as recorded in the RGI.

https://doi.org/10.5194/egusphere-2024-1425
Preprint. Discussion started: 18 June 2024

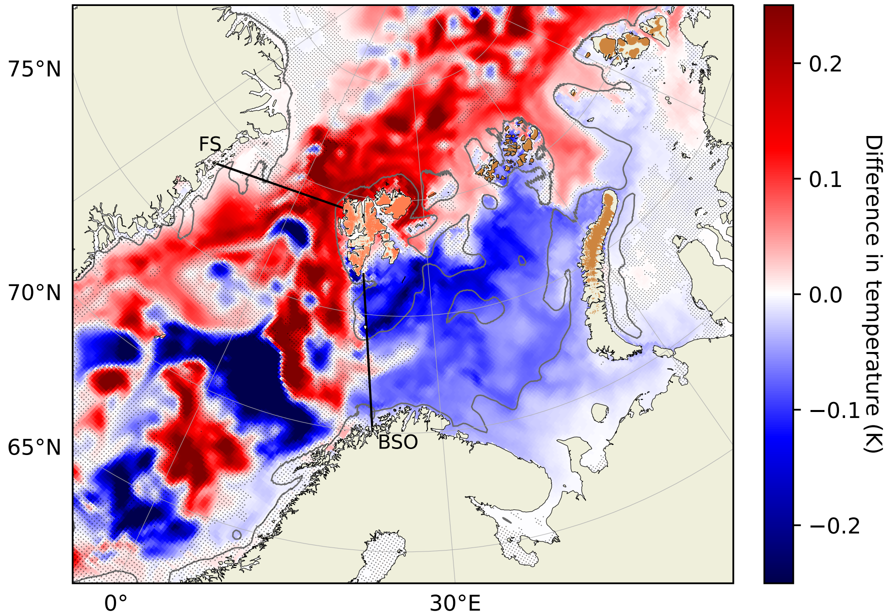

Figure 9. Difference in potential temperature averaged over up to 200 m water depth between the *halfsolid* and the *noOGGM* NEMO runs in the Barents and Nordic Seas area. Dots indicate differences that are not statistically significant, according to Wilcoxon signed-rank tests ($p > 0.05$). FS stands for Fram Strait and BSO for Barents Sea Opening. Colored land area indicates glacierized area as recorded in the RGI. Grey lines show the low-pass filtered 200-m bathymetry contours.

https://doi.org/10.5194/egusphere-2024-1425
Preprint. Discussion started: 18 June 2024

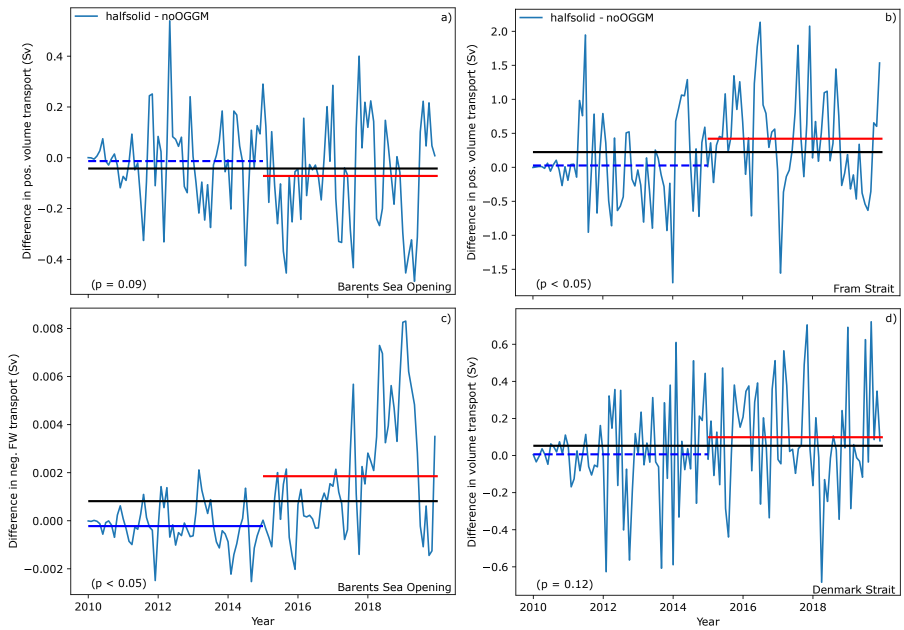

Figure 10. Difference in positive transport through a) the Barents Sea Opening (BSO), and b) Fram Strait (FS), in c) negative freshwater transport through the BSO, and d) total volume transport through Denmark Strait between the *halfsolid* and the *noOGGM* NEMO runs. Positive transport through FS and Denmark Strait mean northward, while positive transport through BSO means eastward. The horizontal lines show average differences over the first (blue) and last (red) five years, as well as over all years (black) of the model integrations. Differences between the two NEMO runs that are statistically significant, according to Wilcoxon signed-rank tests ($p < 0.05$), are drawn as solid lines and dashed otherwise. Values in the lower left corners show the p-values of Wilcoxon signed-rank tests of differences between the differences of the first and last five modeled years.

https://doi.org/10.5194/egusphere-2024-1425
Preprint. Discussion started: 18 June 2024

3.1.4 Arctic Ocean and Sea Ice

We find a band of warmer water in the *halfsolid* run in the eastern part of the Arctic Ocean that follows the shelf break (Arctic Circumpolar Current; see Fig. 11) and is caused by the increased import of Atlantic water through Fram Strait, which was discussed in the previous section. The warm Atlantic water also reaches further north up to the Lomonosov Ridge in the 200-600 m depth range (see Fig. A13). Inspecting differences in salinity, a patch of relatively strongly increased salinity north of the New Siberian Islands is visible (see Fig. A14). In addition, we find an area of decreased SSH around the Mendeleev Ridge, which might point to changes in circulation at the junction of the Beaufort Gyre and the Transpolar Drift (see Fig. A15), although we do not find a coherent pattern of changes in the BSF in that area. The changes in salinity as well as in SSH can be explained by the enhanced Arctic Circumpolar Current, as it blocks the export of fresher water from the Laptev shelf to the interior of the Arctic Ocean, leading to the saltier water from the Atlantic to be accumulated on the East Siberian Shelf and around the Mendeleev Ridge. This is consistent with Figs. A14 and A15 indicating that more freshwater stays on the eastern Arctic shelves, as we see decreased salinity and increased SSH there.

The largest decreases in sea ice thickness between the two NEMO simulation can be found in the western Greenland Sea, north of Svalbard, and in the CAA (Fig. 12). The decrease in sea ice thickness in the former two areas is caused by the changes in the pathway of Atlantic water in the Nordic Seas. Enhanced transport through Fram Strait and enhanced recirculation towards Greenland's east coast increase the advection of heat in these regions (see Fig. 9). Wang et al. (2020) identified a positive feedback, linking an increased import of Atlantic water through Fram Strait to a sea ice decline in that area, which might also play a role here. In the CAA region, we find a similarly strong decrease in sea ice thickness. The smaller increase in upper layer temperature in the CAA compared to the Fram Strait and eastern Greenland areas, suggests that other factors than increased ocean heat content play a role there. The decrease in ice thickness in the CAA is likely also driven by less sea ice advection, since the increase in SSH across the region leads to a divergent flow out of the area (see Figs. 13 and A16). As expected from the higher temperatures in Baffin Bay in the *halfsolid* run, the sea ice is slightly thinner in this area as well. The only area where we find a slightly increased sea ice thickness is between the Barents and Kara Sea, which is most probably related to the decreased heat transport into Barents Sea due to the rerouting of Atlantic water described above. That there is a net sea ice thickness decrease in the northern hemisphere when comparing our two NEMO experiments is intriguing, since we only add freshwater to the ocean, which should not increase its heat content. This points to structural changes in ocean heat (and sea ice) distribution due to the increased freshwater input in the *halfsolid* experiment.

https://doi.org/10.5194/egusphere-2024-1425
Preprint. Discussion started: 18 June 2024

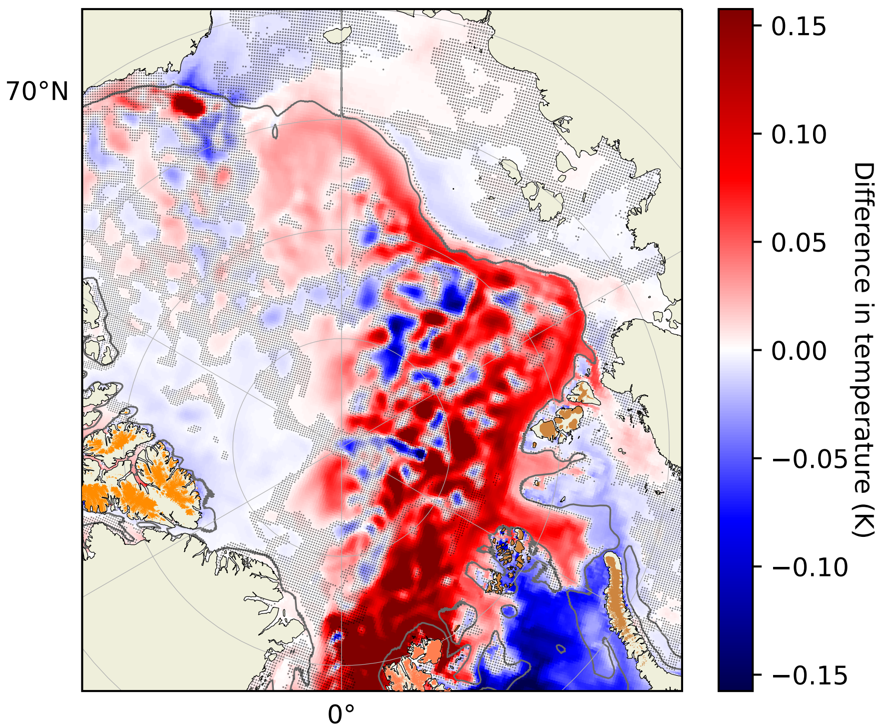

Figure 11. Difference in potential temperature averaged over up to 200 m water depth between the *halfsolid* and the *noOGGM* NEMO runs in the Arctic. Dots indicate differences that are not statistically significant, according to Wilcoxon signed-rank tests (p > 0.05). Colored land area indicates glacierized area as recorded in the RGI. Grey lines show the low-pass filtered 200-m bathymetry contours.

https://doi.org/10.5194/egusphere-2024-1425
Preprint. Discussion started: 18 June 2024

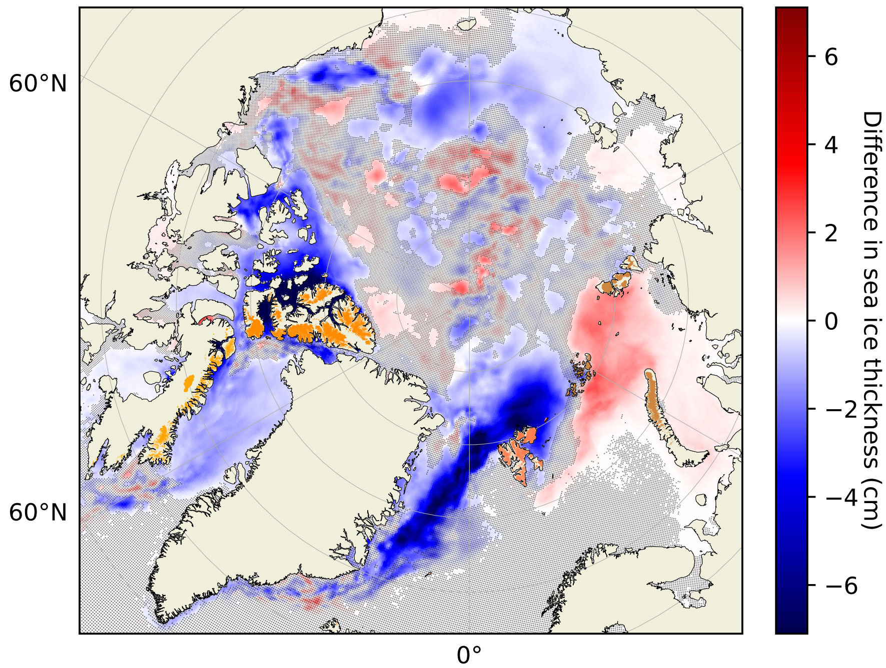

Figure 12. Difference in sea ice thickness between the *halfsolid* and the *noOGGM* NEMO runs. Dots indicate differences that are not statistically significant, according to Wilcoxon signed-rank tests (p > 0.05). Colored land area indicates glacierized area as recorded in the RGI.

https://doi.org/10.5194/egusphere-2024-1425
Preprint. Discussion started: 18 June 2024

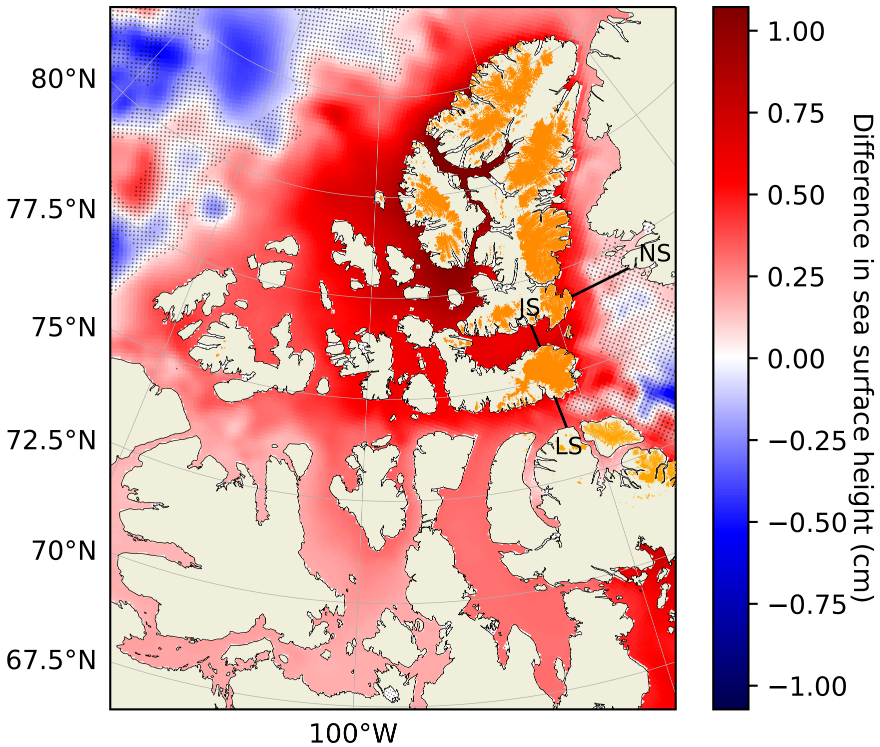

Figure 13. Difference in sea surface height between the *halfsolid* and the *noOGGM* NEMO runs in the CAA region. Dots indicate differences that are not statistically significant, according to Wilcoxon signed-rank tests ($p < 0.05$). Colored land area indicates glacierized area as recorded in the RGI.

https://doi.org/10.5194/egusphere-2024-1425
Preprint. Discussion started: 18 June 2024

3.2 Glacier model

Figure 14 and Table 1 show the results of our OGGM runs with the submarine melt parameterization described above. Submarine melt accounts for between 10 and 27 % of total frontal ablation according to the method we applied, exhibiting a relatively large interquartile range of the results with different valid parameter sets from the latin hypercube sampling. We find the lowest median submarine melt fraction in Arctic Canada North (12 [10, 30] %; value in square brackets is the interquartile range) and the highest in Arctic Canada South (35 [18, 44] %). Note that we exclude Flade Isblink from our results for the Greenland periphery here, as its RGI outlines are erroneous and it maintains an ice shelf (Möller et al., 2022), making the dynamical modeling of it problematic in our framework. Tables 1 and 2 provide an indication of the prevalent frontal ablation mechanisms in the different regions (i.e., submarine melt vs. iceberg calving). That we estimate the largest fraction of frontal ablation caused by submarine melt for the region Arctic Canada South, but the highest thermal forcing for Svalbard, indicates that in the latter region frontal mass loss is more dynamically driven. That is because in OGGM, volume below flotation at the front is removed and added to the calving output variable (i.e., no ice shelves can form). Therefore, if much ice is removed by the flotation criterion, less can be removed by submarine melt when total frontal ablation rates are constrained with observational estimates. The amount of ice above the water level at the front also plays a role here though, since only ice below the water level can be removed by submarine melt.

Table 1 shows that there is no large difference in the submarine melt estimates when applying the thermal forcing derived from the *noOGGM* runs compared to the runs forced with the *halfsolid* NEMO output. This suggests that there are only small coupling effects on glacier mass change over the decadal timescale we investigated here. Tab. 2 shows that the differences in thermal forcing in the vicinity of marine-terminating glaciers are small on average over the last five years of the NEMO integration. We find the largest increase in Svalbard, caused by the rerouting of warm and saline Atlantic water from the southern Barents Sea opening to the Fram Strait, where some of it enters the Barents Sea from the north close to Svalbard (see Fig. 9). This is also the region where we find the strongest increase in submarine melt using the *halfsolid* NEMO run output compared to the *noOGGM* output (see Tab. 1). In contrast, thermal forcing is slightly decreased in the *halfsolid* run in Arctic Canada North and the Russian Arctic. In the latter case this is due to less heat transport from the Atlantic into Barents Sea. Tables 1 and 2 furthermore indicate a perceptible influence of the dependence on water depth of Eq. 2. For example, in Arctic Canada South we find less of an increase in submarine melt at the third than at the first quartile comparing the *halfsolid* to the *noOGGM* NEMO run. This is probably because with stronger submarine melt, we simulate stronger retreat of marine-terminating glacier fronts due to undercutting, which, depending on the submerged bed topography, can decrease the water depth. This leads to a decreased sensitivity to subglacial discharge in Eq. 2, while the amount of subglacial discharge is the same in both OGGM simulations. The Greenland periphery is the only region for which we find a smaller absolute percentage change in submarine melt rates than in thermal forcing (see Tabs. 1 and 2), likely indicating that in this region subglacial discharge has a stronger influence on submarine melt in our model than in the other regions.

Table 3 displays the median and interquartile range of valid parameter sets we found in the different regions as well as the median and interquartile range of the number of valid parameter sets found per glacier. It shows that there are differences

https://doi.org/10.5194/egusphere-2024-1425
Preprint. Discussion started: 18 June 2024

between the regions for the parameters B, β, and to a minor extent A, which are related to the efficiency of heat transfer from the open ocean into the glacier front and the increase of this heat transfer due to subglacial meltwater discharge. Greenland periphery and Arctic Canada South exhibit the largest median (and third quartile) values for A and B. Moreover, we generally found more valid parameter sets for the glaciers in the Greenland periphery and Arctic Canada South. Those findings point to regional differences in the valid parameter ranges and it appears to be the case that the parameter range could be adjusted for the individual regions/glaciers. While our aim in this work was to produce a first estimate of submarine melt of glaciers outside the GrIS, finding more accurate parameter values for the parameterization warrants further investigations in the future.

https://doi.org/10.5194/egusphere-2024-1425
Preprint. Discussion started: 18 June 2024

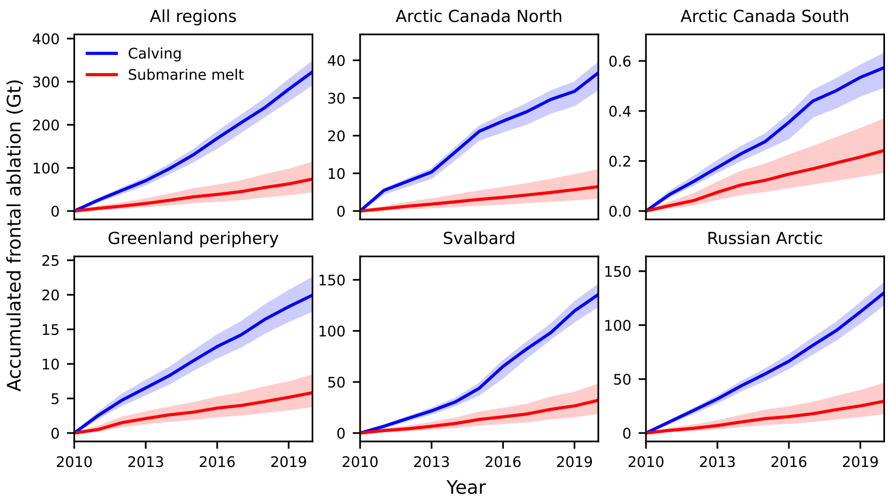

Figure 14. Estimated amounts of the two frontal ablation components submarine melt and calving. Solid lines represent the median and shadings the interquartile range of the valid parameter sets. Note the different scales for the different regions.

Table 1. Estimates of submarine melt rates (median [interquatile range]) between 2015 and 2019 of marine-terminating glaciers in the NEMO-ANHA4 domain. Q_{sm} are submarine melt rates, Q_{fa} the total frontal ablation rates, and ΔQsm the difference in submarine melt rates between the *halfsolid* and the *noOGGM* NEMO runs over the period. n is the number of marine-terminating glaciers in the region.

Region	Q_{sm} (Gt a^{-1})	Q_{sm} / Q_{fa} (%)	ΔQsm (%)	n
03 Arctic Canada North	0.7 [0.4, 1.1]	12 [10, 30]	-2.9 [-2.9, -3.9]	225
04 Arctic Canada South	0.03 [0.02, 0.04]	35 [18, 44]	0.7 [1.1, 0.5]	86
05 Greenland periphery	0.5 [0.3, 0.8]	22 [11, 34]	0.9 [1.2, 1.7]	491
07 Svalbard	3.7 [2.3, 5.5]	19 [10, 27]	6.7 [5.9, 7.0]	163
09 Russian Arctic	3.2 [2.0, 4.9]	16 [11, 27]	-2.7 [-2.6, -2.5]	359
All regions	8.1 [4.9, 12.5]	17 [10, 27]	1.5 [1.3, 1.4]	1325

Table 2. Average of ocean variables in the vicinity of marine-terminating glacier fronts over 2015 to 2019, weighted by submerged frontal cross-section area. T_f is thermal forcing, T potential temperature, S salinity, and d_o the distance-averaged ocean depth of grid cells taken into account for the calculation. The percent difference between the *halfsolid* and the *noOGGM* NEMO runs (i.e., *halfsolid* minus *noOGGM*) is given in the brackets.

Region	T_f (K)	T (°C)	S (PSU)	d_o (m)
03 Arctic Canada North	0.67 (-1.4)	-1.21 (-0.6)	33.0 (-0.1)	236.4
04 Arctic Canada South	0.87 (0.4)	-0.99 (0.6)	32.3 (-0.1)	172.8
05 Greenland periphery	1.61 (1.9)	-0.21 (12.7)	32.7 (-0.0)	145.6
07 Svalbard	2.02 (3.5)	0.13 (128)	34.2 (-0.2)	124.6
09 Russian Arctic	1.19 (-1.7)	-0.74 (-2.6)	34.4 (-0.1)	157.2

https://doi.org/10.5194/egusphere-2024-1425
Preprint. Discussion started: 18 June 2024

Table 3. Ranges (median [interquatile range]) of parameter values in Eq. 2 complying with total frontal ablation estimates from satellite-derived observations (Kochtitzky et al., 2022). n is the median number of valid parameter sets found for individual glaciers in the regions.

Region	A x 10^{-4}	α	B x 10^{-2}	β	n
03 Arctic Canada North	1.5 [0.6, 3.6]	0.48 [0.37, 0.58]	1.5 [0.4, 5.6]	1.53 [1.21, 1.73]	20 [16, 24]
04 Arctic Canada South	1.8 [0.6, 3.9]	0.48 [0.37, 0.58]	2.1 [0.4, 11.0]	1.51 [1.22, 1.73]	25 [19, 25]
05 Greenland periphery	1.8 [0.6, 3.9]	0.48 [0.37, 0.58]	2.1 [0.4, 11.0]	1.51 [1.26, 1.73]	25 [15, 25]
07 Svalbard	1.2 [0.6, 2.4]	0.47 [0.34, 0.57]	0.8 [0.2, 2.1]	1.41 [1.20, 1.66]	10 [4, 13]
09 Russian Arctic	1.5 [0.6, 3.6]	0.48 [0.37, 0.58]	0.8 [0.4, 3.3]	1.46 [1.21, 1.71]	16 [14, 19]

https://doi.org/10.5194/egusphere-2024-1425
Preprint. Discussion started: 18 June 2024

4 Discussion

Comparing our results to those of Castro de la Guardia et al. (2015), whose model setup and scope is quite similar to ours, we find a lower increase in Baffin Bay temperatures (∼0.1 vs. ∼0.3), which can be explained by the smaller increases in sea surface height gradients and stratification, since our additional freshwater input to Baffin Bay is roughly a factor of 5 (50) smaller compared to their experiment with the lowest (highest) additional freshwater forcing along Greenland's west coast. Interestingly, the increase in northward heat transport through Davis Strait we find is higher (1.1 vs 0.5 TW), but the average warming in Baffin Bay is smaller than the differences diagnosed by Castro de la Guardia et al. (2015). This points to the significance of changes associated to an increasing SSH gradient and stratification of Baffin Bay in moderating the temperature response to increased heat influx. The decrease in volume flux through the CAA into Baffin Bay (∼0.8 %) is also small compared to the 9 to 46 % in the experiments demonstrated by Castro de la Guardia et al. (2015). Volume flux through the CAA into Baffin Bay is mainly controlled by the SSH gradients across the straits connecting Baffin Bay to the Arctic Ocean (McGeehan and Maslowski, 2012; Hu and Myers, 2014). This means that these gradients did not change sufficiently to alter the total volume flux between the Arctic and Baffin Bay, comparing our two NEMO experiments, in a notable manner. Our findings are also consistent with those of Lien et al. (2013), linking the effect of changes in SSH around Svalbard to changes in the partitioning of the Atlantic water inflow to the Arctic through the BSO and Fram Strait. Concerning the sea ice thickness differences between our *halfsolid* and *noOGGM* NEMO experiments, it is intriguing that Labe et al. (2018) find a comparatively strong negative trend of sea ice thickness between 1979 to 2015 in some similar areas. These areas are the (north)western Queen Elizabeth Island in the CAA, and north of Svalbard. This might hint at the fact that increased freshwater input from glaciers outside Greenland is a relevant process for sea ice thickness changes.

Placing our results for the SPG area in the context of existing literature, we find that the decrease in SSH and the increase in density of the upper 600 m in the eastern SPG resemble patterns that were linked to an increase in its overall strength (Hakkinen and Rhines, 2004; Chafik et al., 2022; Foukal and Lozier, 2017). The changes in SSH and density could be related to the stronger WGC we find in the *halfsolid* compared to the *noOGGM* run, although an increase in the SPG's overall strength is not directly apparent from the differences in the BSF depicted in Fig. 7. Moreover, the pattern of increased salinity around the northern SPG (see Figs. 6 and A10 panels c)) resembles the pattern found by Born et al. (2016) comparing a strong to a weak mode of the gyre. Thus, we speculate that a relation between the density patterns in the SPG and its circulation features is reflected in our results. The proposed relation is as follows: due to decreased density, in our case caused by increased freshwater input, SSH increases in the Labrador Sea. Now, Chafik et al. (2022) demonstrated that water leaves the Labrador Sea eastwards through two main pathways: either via the rim current that follows the boundary of the SPG, or through the gyre's interior. Hence, the decreased density in the Labrador Sea leads to more of the water that is cooled by surface heat loss, but does not sink, in the Labrador Sea to be accumulated in the eastern SPG together with fresh and cold water from upstream of the Labrador Current (see Figs. 6 and A10 panels d)). In turn, an increased density and decreased SSH in the eastern SPG causes more Atlantic water to move around the gyre's eastern part and towards the Labrador Sea. Sun et al. (2021) proposed oscillating feedbacks of the SPG's strength and the deep convection in the Labrador Sea, asserting that an

https://doi.org/10.5194/egusphere-2024-1425
Preprint. Discussion started: 18 June 2024

increased gyre strength leads to an increased density transport into the Labrador Sea, in turn, increasing the deep convection. This would decrease SSH in the Labrador Sea and the export of cooled water to the gyre's interior. In panels a) and b) of Fig. 6, some areas of the northeastern Labrador Sea indeed show a slightly higher density and mixed layer depth, hinting at this feedback potentially being in effect. While, as stated above, the changes in mixed layer depth we found are relatively small, and our findings regarding BSF differences are not straightforward, the coherence of our findings with mechanisms linking Labrador Sea deep convection and the SPG's strength presented in previous publications is intriguing. Further research might be conducted investigating whether the positive feedback of the oscillation mechanism proposed by Sun et al. (2021) can offset increased freshwater input over a longer time span.

Although our rather simple approach is sufficient to produce first estimates of the coupling effects between OGGM and NEMO on a decadal timescale, we now lay out some aspects that could be improved in future works on the subject of northern hemisphere ice-ocean interactions outside the GrIS. Concerning the aspect of using OGGM output as an input for NEMO, it is arguable whether putting the meltwater runoff and calving estimates derived from OGGM simply into the NEMO grid cell nearest to the glacier terminus is a sound approach. Particularly in regions with complex topography and/or fjord systems, as for example the CAA, more sophisticated routing approaches might be advisable. Also, whether the *halfsolid* assumption is valid for regions outside Greenland needs to be investigated, since it is not clear how much of the iceberg mass actually melts within the fjords before the icebergs reach the open ocean/NEMO grid cell. When differentiating between solid and liquid discharge, the amount of submarine melt should be taken into account as well. Moreover, there might be other hydrological changes in glacierized areas, as, for example, more liquid and less solid precipitation, which might change the runoff from such regions systematically and should thus be included in the (baseline) freshwater forcing in future studies. Additionally, the baseline runoff and the Bamber et al. (2018) data not covering the whole modeling period, might induce some uncertainty in our results, since the impact of the additional freshwater we examined could be altered. If, for instance, the ratio of the additional freshwater in the *halfsolid* run to the baseline plus Greenland runoff was larger (smaller), the impact would presumably be larger (smaller) as well. Ultimately, we did not aim to produce as accurate hindcasts as possible, but to obtain first estimates of the coupling effects between OGGM and NEMO, for which we consider a somewhat idealized setup appropriate.

We implicitly assume that the amount of submarine melt of glaciers outside the GrIS is so small that the amount of heat drained from the ocean necessary to produce this melt is negligibly small for the ocean heat budget. A rough estimate yields that approx. 2.9 x 10^{18} J a^{-1} would be needed for our median estimate of 8.1 Gt a^{-1} submarine melt. This is three orders of magnitude smaller than the estimated annual ocean heat uptake due to anthropogenic climate change (Cheng et al., 2022), indicating that the impact of submarine melt from glaciers outside the ice sheets is small on the global scale of the ocean heat budget, though it might be relevant on a local scale. Similarly, it would be interesting to see what the effect of adjusting the freshwater input's temperature to values different from the ocean surface temperatures are. Especially glacial meltwater might actually be colder, and thus such an adjustment might have an influence on the model results. Moreover, it might be the case that the increased surface layer mixing in all NEMO grid cells where we add liquid freshwater to the ocean is inaccurate. That is because in reality, the glacial meltwater is injected into the fjords, which is some distance apart from the open ocean, and the meltwater might be stored in the fjords for some time before being released to the ocean (Straneo and Cenedese, 2015;

https://doi.org/10.5194/egusphere-2024-1425
Preprint. Discussion started: 18 June 2024

Sanchez et al., 2023). Thus, increased surface mixing might not actually occur at the open ocean locations where it is added to the NEMO-ANHA4 grid in our simulations.

Another aspect that could be improved regarding the modeling approach is the resolution of the ocean model, because the NEMO-ANHA4 setup is probably too coarse to yield a good representation of ocean eddies, which is of importance for processes in, e.g., the Labrador Sea (Pennelly and Myers, 2022), the Fram Strait (Hattermann et al., 2016), and the Arctic Circumpolar Current (Athanase et al., 2021). Furthermore, employing a fully coupled ocean-atmosphere model could provide insights into how ocean-atmosphere interactions might modulate the findings described in this work. Applying (passive) tracers in future studies could furthermore reveal where the meltwater from the glaciers moves in the ocean. Employing water mass descriptions in the temperature and salinity fields could facilitate a more targeted analysis of specific Atlantic-Arctic exchanges that are influenced by glacier melt from outside the GrIS. Finally, longer model runs would provide insights into whether the accumulation of freshwater from glacier melt outside of Greenland could at some point influence the AMOC either directly due to density changes at deep water formation sites or mechanisms linked to the reduction of Arctic sea-ice cover (Sévellec et al., 2017), and whether the impacts we found persist on longer timescales. Combining the mentioned potential improvements with a longer integration time of NEMO would consolidate knowledge about the influence of glaciers outside the GrIS on the ocean circulation and make sure potential initial adjustment/spin-up effects have fully abated.

The spin-up of the ocean model has two main aspects. Firstly, the model is initialized with ocean reanalysis data, and forced by atmospheric reanalysis data. Since even in more recent times observations of the deep ocean are sparse, the initial conditions might be inconsistent with the model physics. Additionally, the initial conditions might be inconsistent with the atmospheric forcing. This means that the modeled ocean state adjusts to these inconsistencies in what can be called an initialization shock, which levels off relatively quickly in our setup though (see Fig. A17). Any remaining drift due to initialization will be similar in our two setups, thus likely not hindering a meaningful comparison between them regarding the impact of increased freshwater input at the surface. The second aspect is the accumulation of this additional freshwater in the ocean. The larger freshwater input in the *halfsolid* will have an increasingly strong effect over time, while the ocean (model) adjusts to this forcing. An indication of both our model setups starting to follow their own trajectory after the first half of the modeled period is that differences between them shown in Figs. 3 and 10 are not statistically significant in the first five years, but they are in the second five years. Naturally, it would be beneficial to cover longer time spans, in order to avoid compounding effects of internal variability and the imposed forcing. For instance, during our chosen modeling period, there were periods of freshening (2012-'16; Holliday et al., 2020) and cooling/warming (2014-'16/2016-'18; Desbruyères et al., 2021) in the subpolar North Atlantic due to natural variability on (multi-)decadal timescales. These might modify the ocean's response to the difference in freshwater forcing between our two NEMO experiments. Especially the mechanism described by Holliday et al. (2020), linking the aforementioned freshening to changes in the Labrador Current's pathway due to wind-stress forcing, could have an impact on the distribution of the freshwater added to the current upstream. The issue of natural variability might also be related to why we see a change in the sign of the differences in the WGC currents' strength between our two model setups after the first five years (see Fig A6). Generally, spin-up refers to a procedure that brings a general circulation model (close) to an equilibrium state, and this is particularly intricate for the deep ocean. In this study, we examined an ocean perturbed

https://doi.org/10.5194/egusphere-2024-1425
Preprint. Discussion started: 18 June 2024

by anthropogenic climate change, and did not focus on the deep ocean. Moreover, we start the model from contemporaneous conditions, which should be relatively well constrained for the upper ocean. Therefore, we argue that ten years of model run, considering the first five years as spin-up, is suitable for a first-order estimate of the ice-ocean interactions near the surface that we studied. Still, it should be investigated in future studies whether running the model with constant forcing over several years and then switching to the actual forcing timeseries would significantly alter the findings.

On the side of OGGM, it became apparent from Table 3 that the parameter ranges sampled with the latin hypercube approach should be adjusted for individual regions. Xu et al. (2013) also suggest that the parameter values might actually differ between (high and low) subglacial discharge regimes. Moreover, the parameters in Eq. 2 probably depend on processes like subglacial hydrology and frontal plume formation, fjord circulation and subglacial discharge's effect on it, and on fjord-ocean water interchange as well as on the fjord geometry. As we find the largest regional differences in the parameters that control the efficiency of heat transfer from the open ocean into the glacier front in the absence of subglacial discharge (B and β), the differences in parameter values might be best explained by differences in fjord properties and fjord-ocean exchange. Since resolving individual fjords in an ocean circulation model would necessitate a very fine spatial resolution, it is too computationally expensive to run such a setup for all the relevant fjords and longer time periods. This points to the fact the fjord water properties in relation to open ocean water properties and subglacial discharge need to be better understood and incorporated in models in order to better constrain the involved parameters. Another aspect that could be further investigated concerning the submarine melt parameterization is which part of the ocean in the marine-terminating glaciers' vicinity should be used to source the thermal forcing from before inserting it in Eq. 2. Refining the distance from the glacier termini as well as the ocean depth range that should be taken into account could help to better constrain submarine melt estimates. Furthermore, dynamically modeling marine-terminating glaciers requires additional parameters compared to land-terminating glaciers that need to be constrained and might be interrelated. For instance, the frontal ablation parameter (k) depends on the choice of values for the parameters involved in the modeling of ice dynamics, since these parameters control the initial geometry given by the ice thickness inversion as well as the dynamical mechanisms of frontal ablation (Malles et al., 2023). This means that when aiming at most accurately simulating (frontal) ice dynamics, such parameters need to be better constrained, although this was not the aim in this work.

An obvious next step is the continuation of the simulations into future projections, since glacier mass loss is projected to increase in the future and hence the impact of increased freshwater input can be expected to grow (Marzeion et al., 2020). For this, a coupling scheme that updates the forcings between the models, for example in the form of a decadal step-coupling, would have to be developed. Regarding projections of future glacier mass loss, it would be interesting to investigate how future changes of ocean properties (different from the effects caused by the meltwater) will influence projected frontal ablation rates. For example, increased thermal forcing in combination with increased subglacial discharge would increase submarine melt rates, which might lead to stronger undercutting and thus accelerated retreat (Wood et al., 2021, 2018). On the other hand, the number of marine-terminating glaciers outside the GrIS is already decreasing and projected to continue decreasing in the future (Kochtitzky et al., 2022; Malles et al., 2023), which might attenuate the potential increase in submarine melt.

https://doi.org/10.5194/egusphere-2024-1425
Preprint. Discussion started: 18 June 2024

5 Conclusions

We have presented the first investigation of ice-ocean interactions in the northern hemisphere outside the GrIS, applying one-way coupling of an ocean general circulation model (NEMO-ANHA4) and a glacier evolution model (OGGM) for the years 2010 to 2019. On the ocean side, we found that the NEMO simulation forced with freshwater input derived from glacier mass loss estimates given by OGGM showed considerable differences to the experiment solely forced with freshwater input from the GrIS. Consistent with what has been found in a previous study on the influence of increased freshwater input from the western GrIS on Baffin Bay, we found an increased ocean heat content in this region. We also found changes in the Nordic Seas that were brought about by the increased freshwater input around Svalbard and the Russian Arctic and lead to a decreased transport of Atlantic water into the Barents Sea, causing this water to be rerouted through Fram Strait into the Arctic. Furthermore, we find sea surface height changes in the Baffin Bay, the CAA, the Nordic Seas, the subpolar gyre and even in the Arctic Ocean that indicate changes in (gyre) circulation patterns across the northern hemisphere. Concerning the AMOC, our results do not suggest a significant change and the decrease in mixed layer depth over the Labrador Sea region in the OGGM-forced NEMO simulation falls within the range of interannual and model variability. Regarding the Arctic Ocean, an intrusion of rerouted warm Atlantic water through Fram Strait leads to a band of warmer water along the eastern shelf break. This rerouting of Atlantic water also goes along with a decrease in sea ice thickness in the Fram Strait region and north of Svalbard. We also find a comparatively strong decrease in sea ice thickness in the Canadian Arctic Archipelago. In total, sea ice thickness is decreased in the northern hemisphere when including freshwater forcing from glacial melt outside the GrIS.

Concerning the influence of the oceanic forcing on glacier mass loss, we find that for marine-terminating glaciers in the domain of the NEMO-ANHA4 configuration, submarine melt accounts for a median 17 % ($\approx$8.1 Gt a^{-1}) of frontal ablation throughout the spun-up simulation period (2015 to 2019), with an interquartile range of 10 to 27 % ($\approx$4.9 to 12.5 Gt a^{-1}). The increase in submarine melt when applying the thermal forcing from the NEMO experiment that includes freshwater input from the OGGM glaciers, compared to the experiment that does not include it, is very small (1.5 [1.3, 1.4] %). The only region where we find a notable increase of submarine melt is Svalbard. This is caused by the rerouting of warm Atlantic water through Fram Strait, which thereby reaches Svalbard from the north. On the other hand, we find a slight decrease in Arctic Canada North and the Russian Arctic. Our results suggest that the parameter ranges applied in the latin hypercube sampling of the estimated parameter space should be adjusted for the individual regions, as we find less viable parameter sets for individual glaciers in some regions than in others, when applying the same ranges for all regions.

Future studies investigating northern hemisphere ice-ocean interactions could improve several aspects of this work. Using a (more rigorously spun-up) higher resolution ocean model configuration and analyzing passive tracer movements could yield stronger insights into the impact of increased freshwater input from glacier mass loss outside the GrIS on ocean circulation. Additionally, advancing the simulations into future projections would be crucial in gaining a better understanding of potential future changes in the ocean as well as in glacier mass changes due to ice-ocean interactions. This would necessitate an actual two-way coupling of the models, for example in the way of a decadal step-coupling. Another approach could be to conduct decadal snapshot simulations similar to what was presented in this work, but for a future period in which the melt signal from

https://doi.org/10.5194/egusphere-2024-1425
Preprint. Discussion started: 18 June 2024

northern hemisphere glaciers outside Greenland will be larger. Applying a more thorough approach of injecting the glacial meltwater into the ocean in terms of the routing from the glacier termini, the temperature and depth at which it is injected, and the way it changes mixing in the ocean model might help to improve the accuracy of coupled simulations.

Code and data availability. The NEMO documentation and model code are available at https://www.nemo-ocean.eu/ (last access: 03 May 2024, Madec et al. (2016)). The documentation of the OGGM model is available at https://docs.oggm.org/en/v1.5.3/ (last access: 03 May 2024), and the modified code including the submarine melt parameterization can be accessed through Zenodo (doi: 10.5281/zenodo.10468696). The output files of both models used to write this manuscript are available on Zenodo as well (doi: 10.5281/zenodo.10468082).

https://doi.org/10.5194/egusphere-2024-1425
Preprint. Discussion started: 18 June 2024

Appendix A

A1

https://doi.org/10.5194/egusphere-2024-1425
Preprint. Discussion started: 18 June 2024

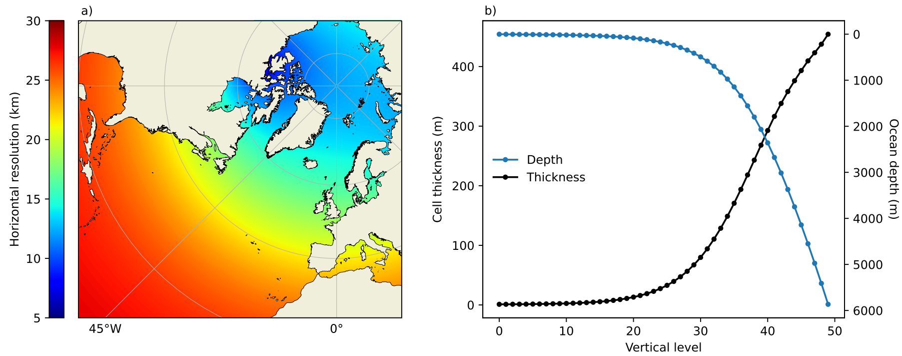

Figure A1. Grid characteristics of the NEMO-ANHA4 configuration. a): horizontal resolution, b): vertical cell thicknesses of the 50 levels (black), and corresponding ocean depth (blue).

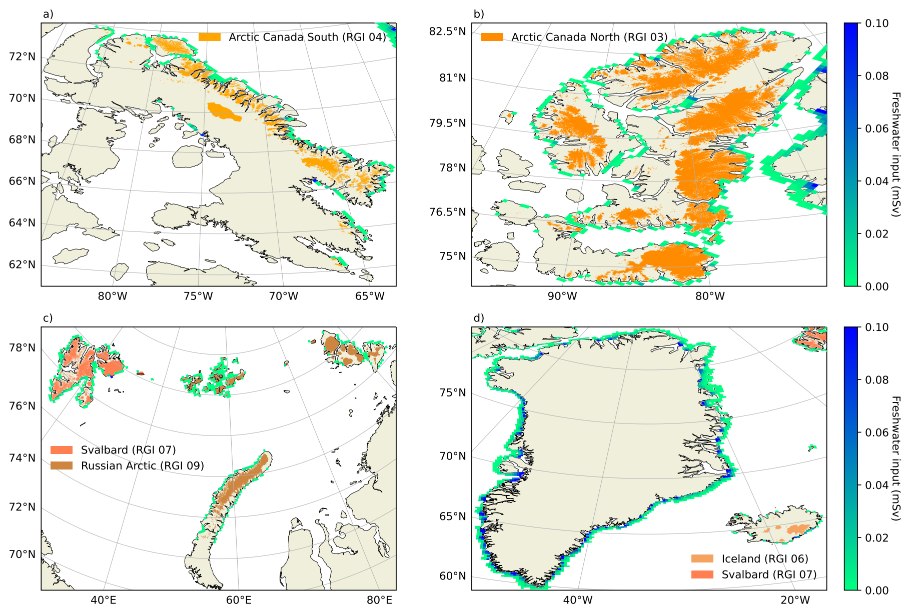

Figure A2. Distribution of liquid freshwater input in the *halfsolid* NEMO run setup (2010 to 2019 average), apart from the baseline continental runoff derived from Dai et al. (2009). Regions shown are: a) Baffin Island, b) Queen Elizabeth Island ("CAA"), c) Barents and Kara Sea, and d) Greenland and Iceland. In the *noOGGM* run setup only the runoff around Greenland, displayed in panel d) and derived from Bamber et al. (2018), is an additional input to the ocean. Colored land areas indicate the named glacierized regions as recorded in the RGI.

https://doi.org/10.5194/egusphere-2024-1425
Preprint. Discussion started: 18 June 2024

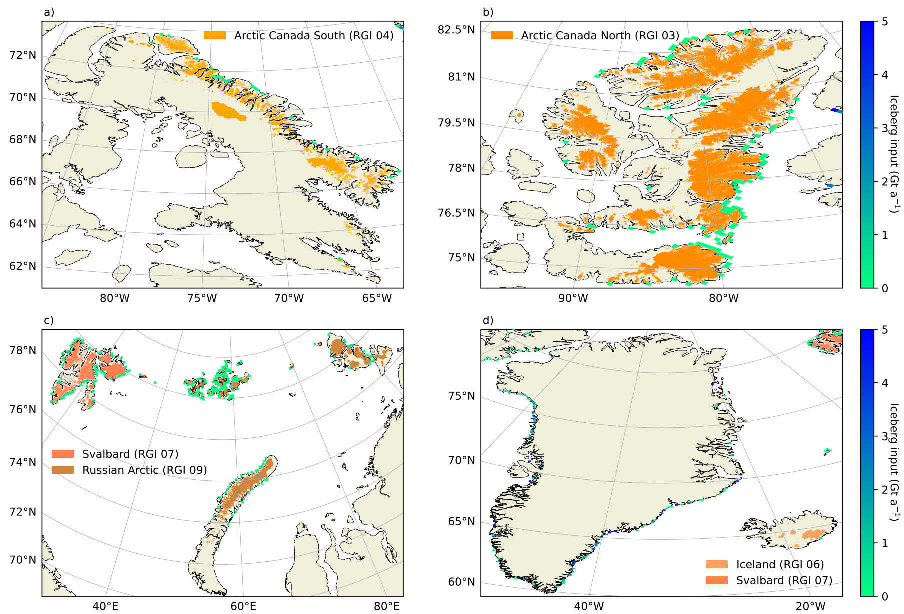

Figure A3. Iceberg input distribution in the *halfsolid* NEMO run setup (2010 to 2019 average). Regions shown are: a) Baffin Island, b) Queen Elizabeth Island ("CAA"), c) Barents and Kara Sea, and d) Greenland and Iceland. In the *noOGGM* run setup only the icebergs around Greenland, displayed in panel d) and derived from Bamber et al. (2018), are added to the ocean. Colored land areas indicate the named glacierized regions as recorded in the RGI.

https://doi.org/10.5194/egusphere-2024-1425
Preprint. Discussion started: 18 June 2024

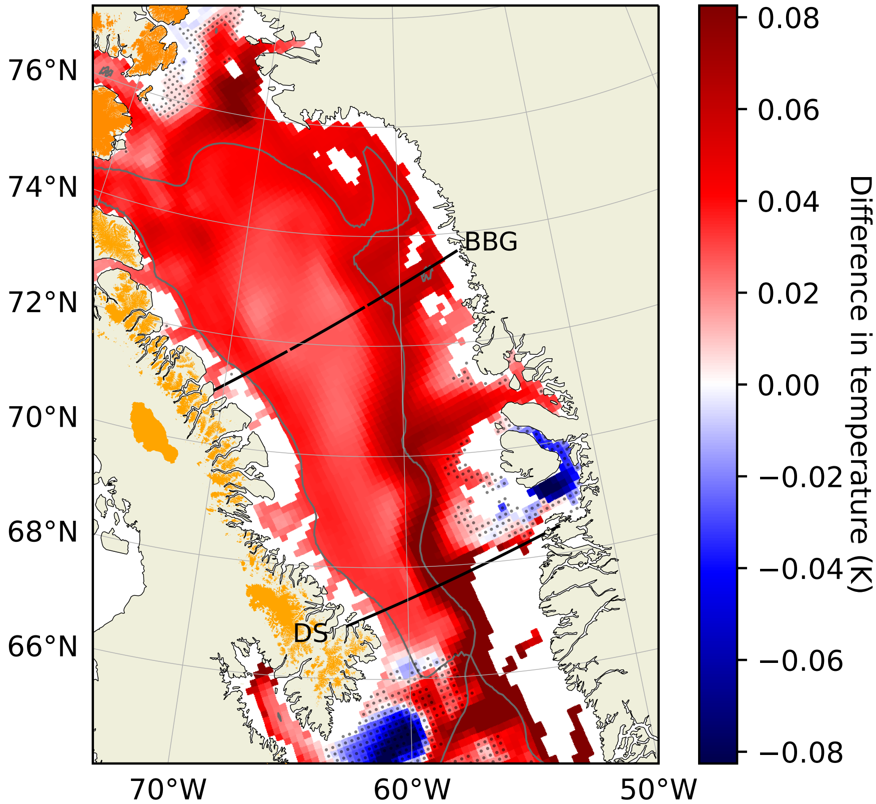

Figure A4. Difference in potential temperature averaged over 200-600 m water depth between the *halfsolid* and the *noOGGM* NEMO runs in Baffin Bay. Dots indicate differences that are not statistically significant, according to Wilcoxon signed-rank tests (p > 0.05). BBG stands for the Baffin Bay Gyre section and DS for the Davis strait section. Colored land area indicates glacierized area as recorded in the RGI. Grey lines show the low-pass filtered 600-m bathymetry contours.

https://doi.org/10.5194/egusphere-2024-1425
Preprint. Discussion started: 18 June 2024

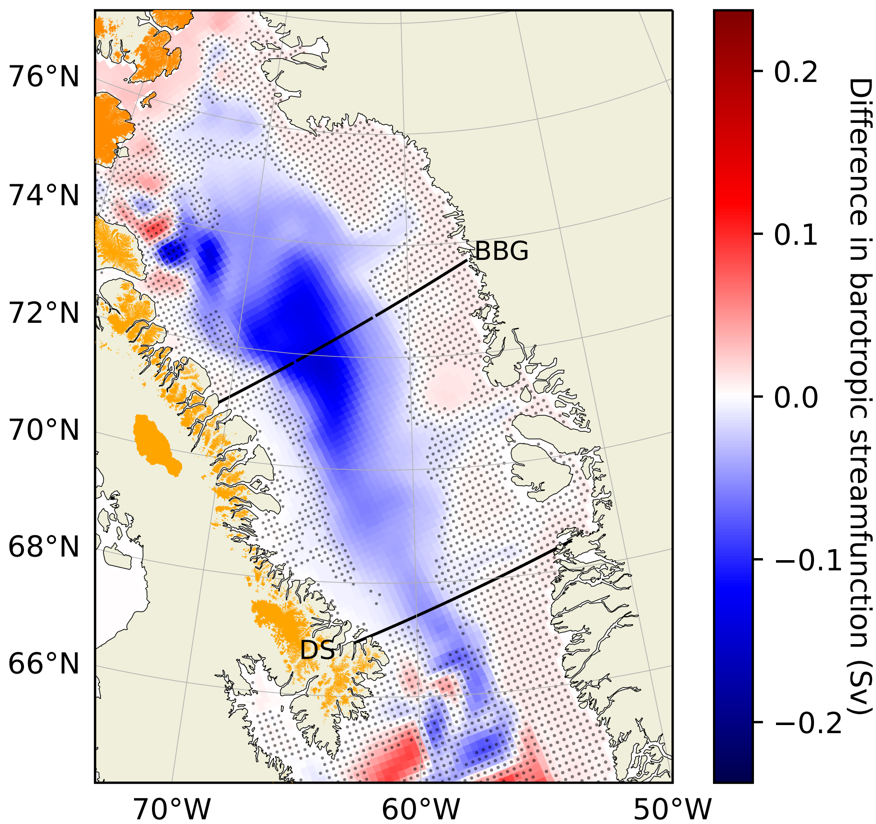

Figure A5. Difference in barotropic streamfunction between the *halfsolid* and the *noOGGM* NEMO runs in the Baffin Bay area. Dots indicate differences that are not statistically significant, according to Wilcoxon signed-rank tests (p > 0.05). Colored land area indicates glacierized area as recorded in the RGI.

https://doi.org/10.5194/egusphere-2024-1425
Preprint. Discussion started: 18 June 2024

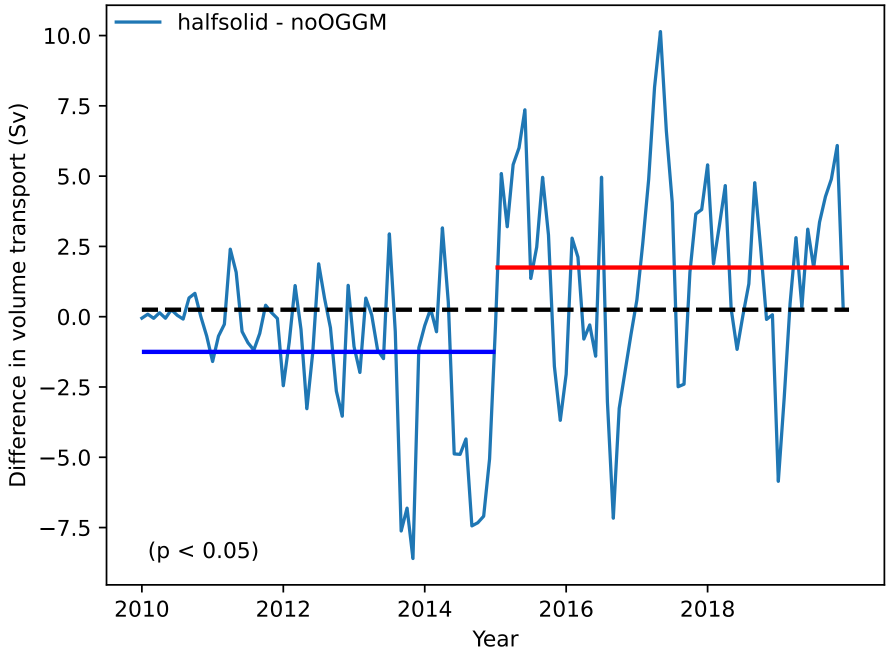

Figure A6. Differences in WGC volume transport at Cape Desolation. The horizontal line shows the average difference over the first (blue) and last (red) five years, as well as over all years (black) of the model integrations. Differences between the two NEMO runs that are statistically significant, according to Wilcoxon signed-rank tests ($p < 0.05$), are drawn as solid lines and dashed otherwise. Values in the lower left corners show the p-values of Wilcoxon signed-rank tests of differences between the differences of the first and last five modeled years.

https://doi.org/10.5194/egusphere-2024-1425
Preprint. Discussion started: 18 June 2024

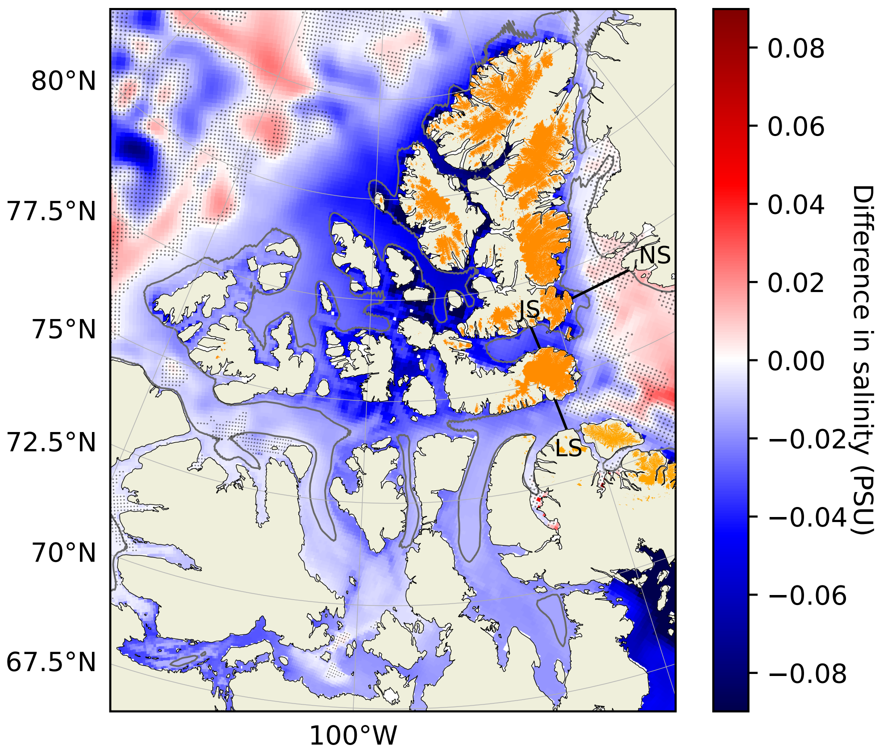

Figure A7. Difference in salinity averaged over up to 200 m water depth between the *halfsolid* and the *noOGGM* NEMO runs in the CAA region. Colored land area indicates glacierized area as recorded in the RGI. Grey lines show the low-pass filtered 200-m bathymetry contours.

https://doi.org/10.5194/egusphere-2024-1425
Preprint. Discussion started: 18 June 2024

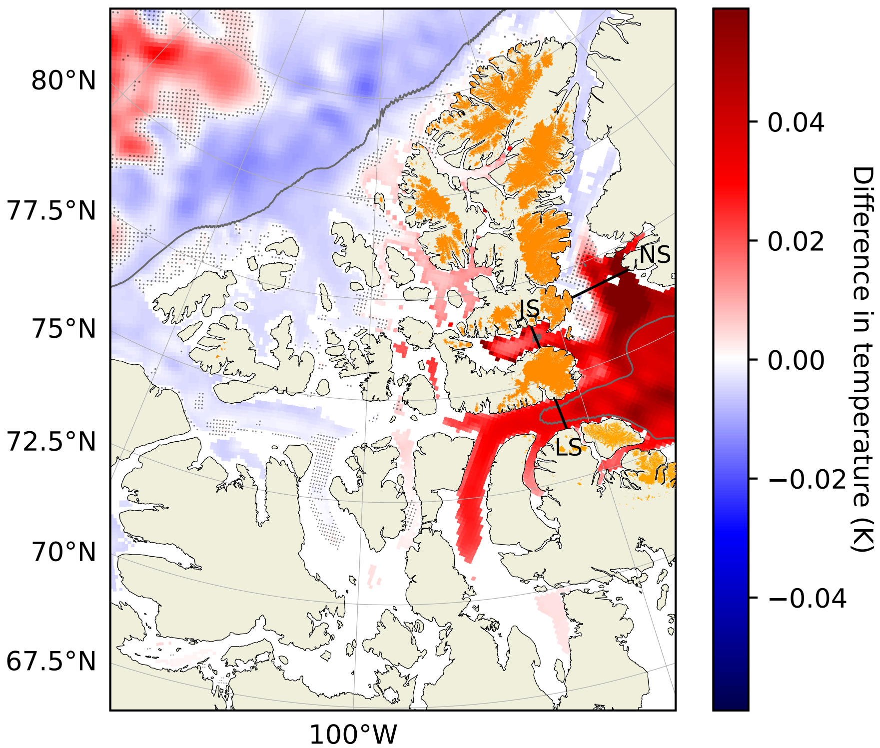

Figure A8. Difference in potential temperature averaged over 200-600 m water depth between the *halfsolid* and the *noOGGM* NEMO runs in the CAA region. NS stands for the Nares Strait, JS for the Jones Sound, and LS for the Lancasters sound section. Dots indicate differences that are not statistically significant, according to Wilcoxon signed-rank tests ($p > 0.05$). Colored land area indicates glacierized area as recorded in the RGI. Grey lines show the low-pass filtered 600-m bathymetry contours.

https://doi.org/10.5194/egusphere-2024-1425
Preprint. Discussion started: 18 June 2024

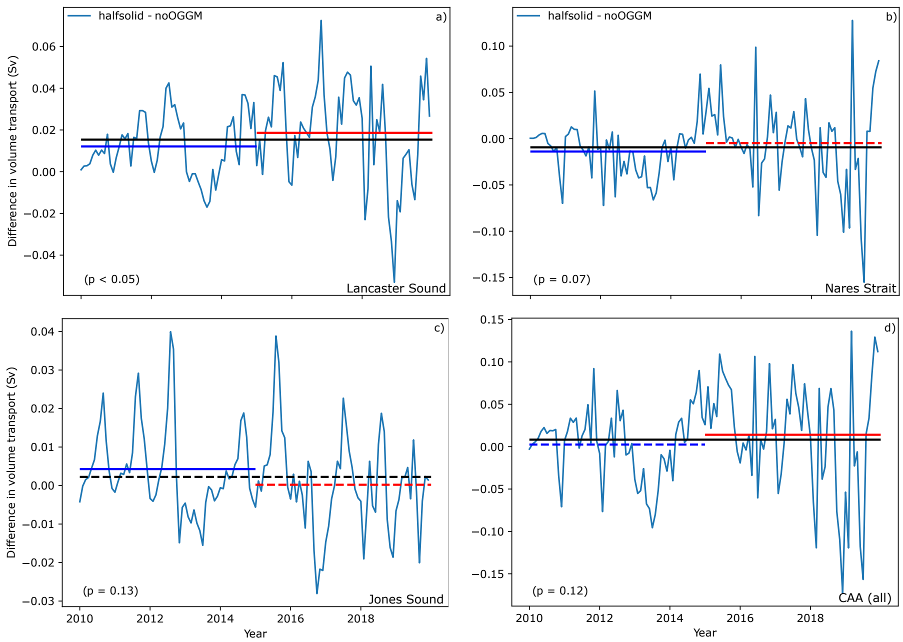

Figure A9. Differences in volume transport through the three main ocean pathways connecting the CAA and Baffin Bay (a-c), and d) the volume transport through all three. Note that volume flux northward through the CAA is defined as positive. The horizontal lines show average differences over the first (blue) and last (red) five years, as well as over all years (black) of the model integrations. Differences between the two NEMO runs that are statistically significant, according to Wilcoxon signed-rank tests ($p < 0.05$), are drawn as solid lines and dashed otherwise. Values in the lower left corners show the p-values of Wilcoxon signed-rank tests of differences between the differences of the first and last five modeled years.

https://doi.org/10.5194/egusphere-2024-1425
Preprint. Discussion started: 18 June 2024

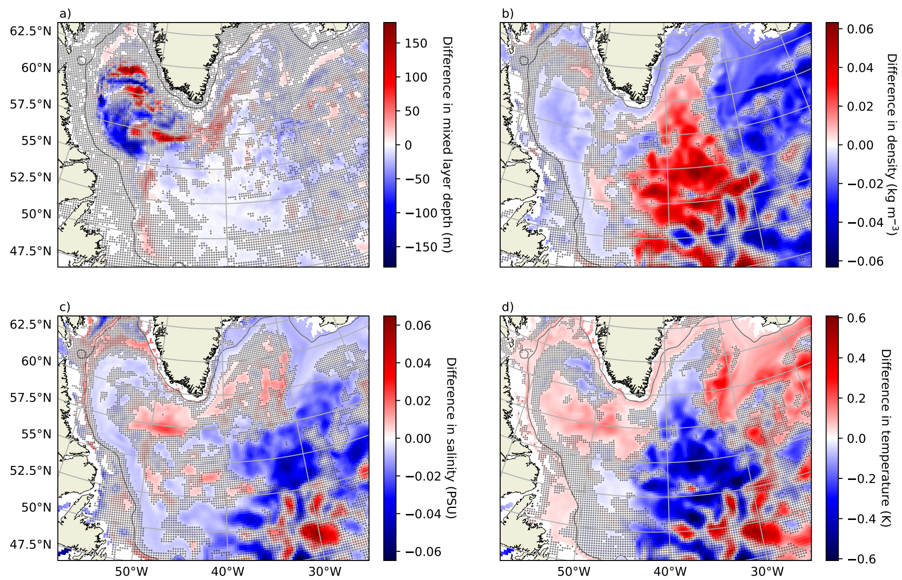

Figure A10. Difference in a) mixed layer depth, b) density, c) salinity, and d) potential temperature averaged over 200-600 m water depth between the *halfsolid* and the *noOGGM* NEMO runs in the supolar gyre region. Dots indicate differences that are not statistically significant, according to Wilcoxon signed-rank tests (p > 0.05). Grey lines show the low-pass filtered 600-m bathymetry contours.

https://doi.org/10.5194/egusphere-2024-1425
Preprint. Discussion started: 18 June 2024

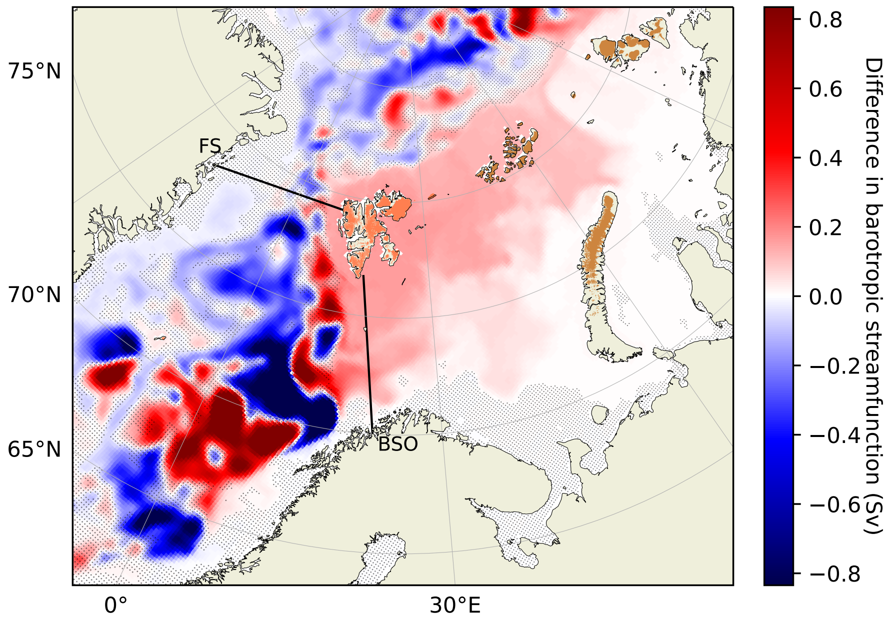

Figure A11. Difference in barotropic streamfunction between the *halfsolid* and the *noOGGM* NEMO runs in the Barents and Nordic Seas area. Dots indicate differences that are not statistically significant, according to Wilcoxon signed-rank tests ($p > 0.05$). Colored land area indicates glacierized area as recorded in the RGI.

https://doi.org/10.5194/egusphere-2024-1425
Preprint. Discussion started: 18 June 2024

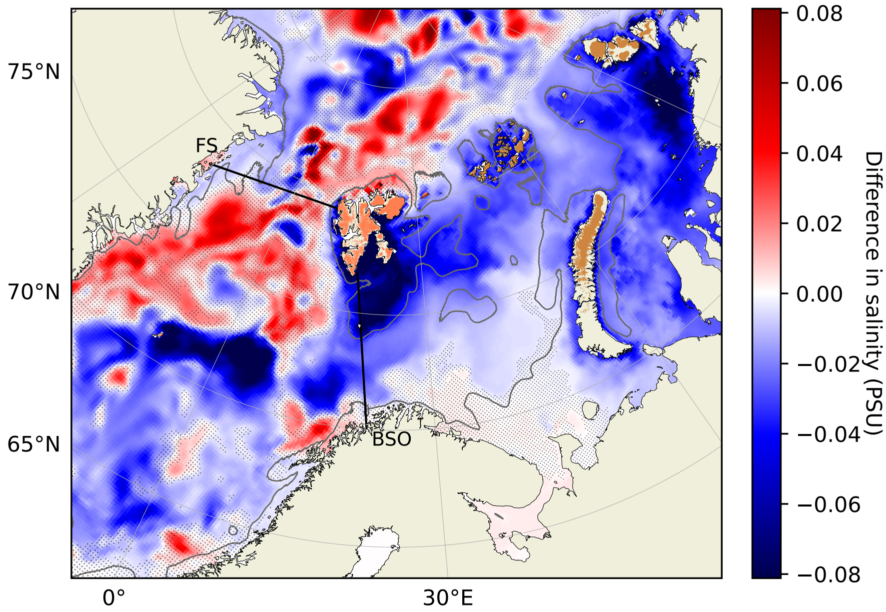

Figure A12. Difference in salinity averaged over up to 200 m water depth between the *halfsolid* and the *noOGGM* NEMO runs in the Barents and Nordic Seas area. Dots indicate differences that are not statistically significant, according to Wilcoxon signed-rank tests ($p > 0.05$). Colored land area indicates glacierized area as recorded in the RGI. Grey lines show the low-pass filtered 200-m bathymetry contours.

https://doi.org/10.5194/egusphere-2024-1425
Preprint. Discussion started: 18 June 2024

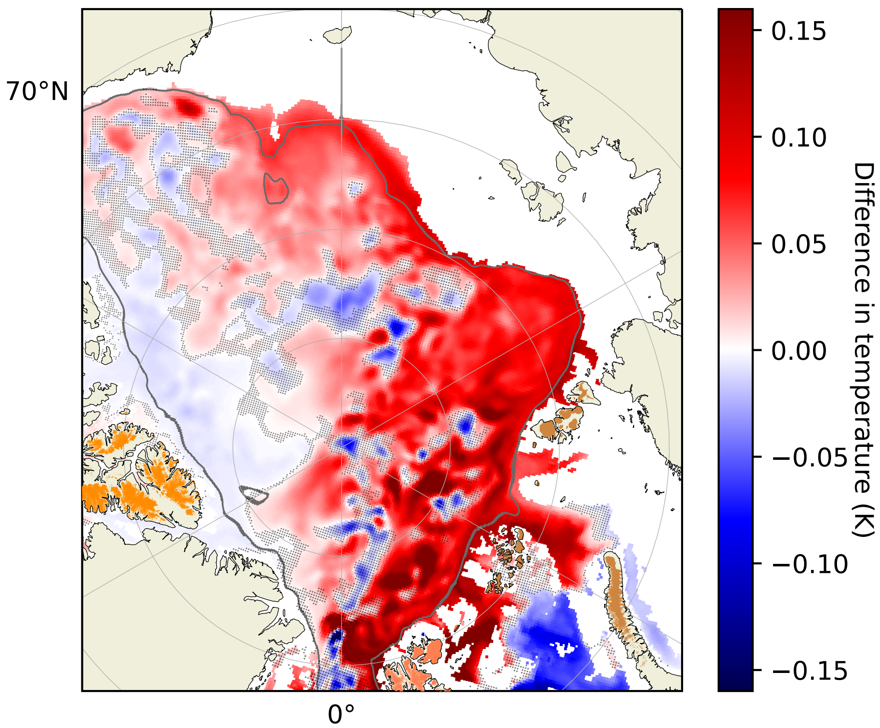

Figure A13. Difference in potential temperature averaged over 200-600 m water depth between the *halfsolid* and the *noOGGM* NEMO runs in the Arctic. Dots indicate differences that are not statistically significant, according to Wilcoxon signed-rank tests ($p < 0.05$). Colored land area indicates glacierized area as recorded in the RGI. Grey lines show the low-pass filtered 600-m bathymetry contours.

https://doi.org/10.5194/egusphere-2024-1425
Preprint. Discussion started: 18 June 2024

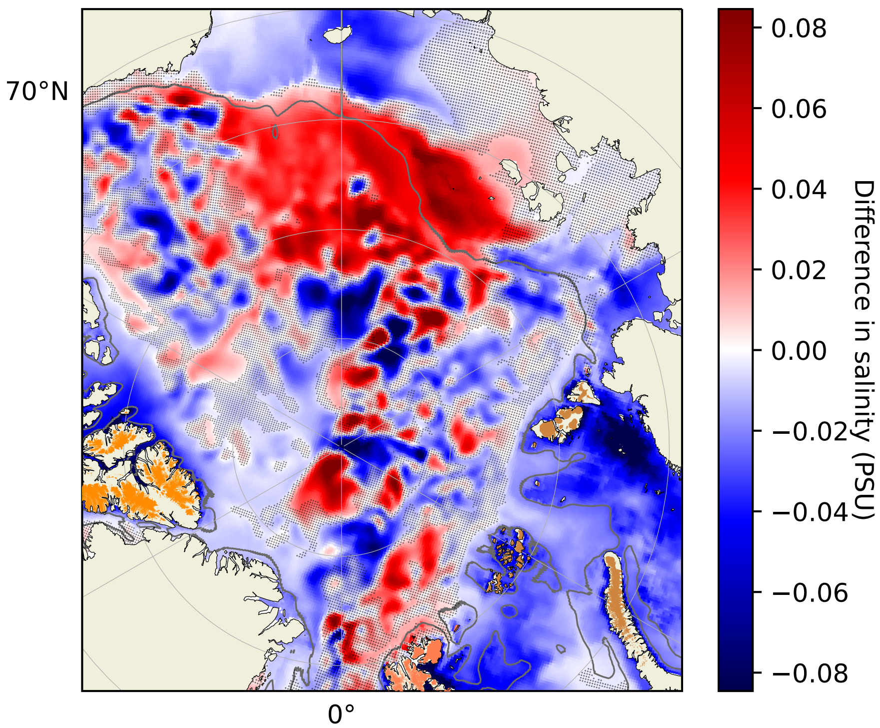

Figure A14. Difference in salinity averaged over up to 200 m water depth between the *halfsolid* and the *noOGGM* NEMO runs in the Arctic. Dots indicate differences that are not statistically significant, according to Wilcoxon signed-rank tests ($p < 0.05$). Colored land area indicates glacierized area as recorded in the RGI. Grey lines show the low-pass filtered 200-m bathymetry contours.

https://doi.org/10.5194/egusphere-2024-1425
Preprint. Discussion started: 18 June 2024

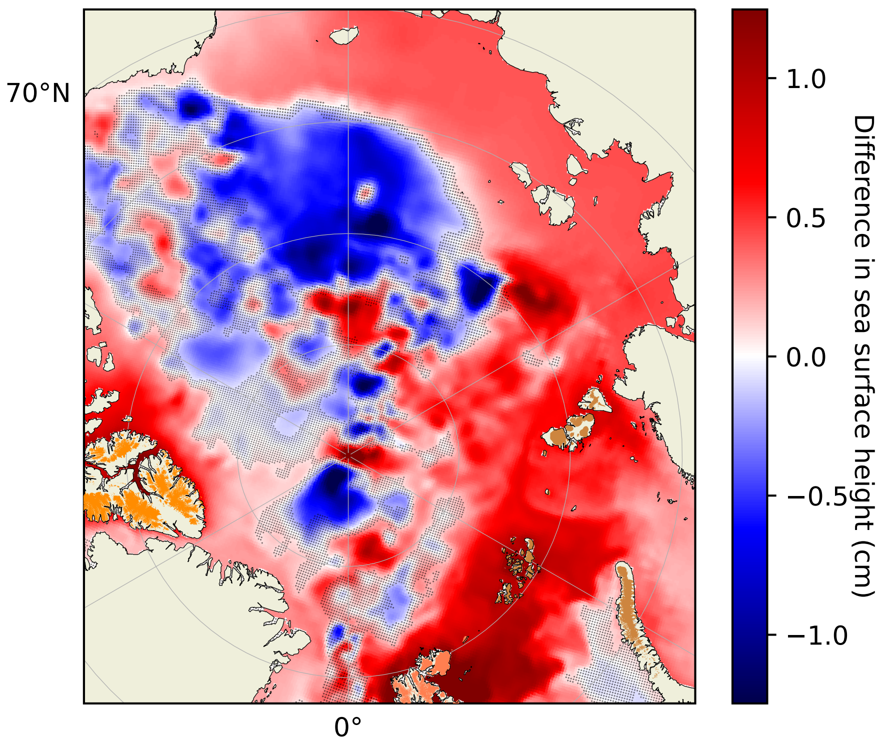

Figure A15. Difference in sea surface height between the *halfsolid* and the *noOGGM* NEMO runs in the Arctic. Dots indicate differences that are not statistically significant, according to Wilcoxon signed-rank tests ($p < 0.05$). Colored land area indicates glacierized area as recorded in the RGI.

https://doi.org/10.5194/egusphere-2024-1425
Preprint. Discussion started: 18 June 2024

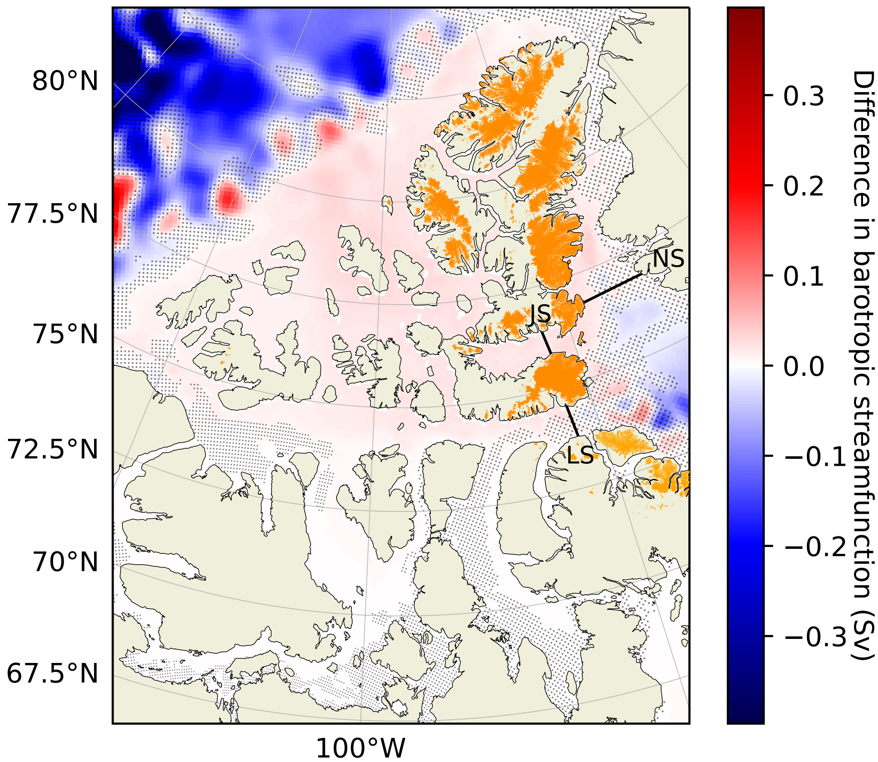

Figure A16. Difference in barotropic streamfunction between the *halfsolid* and the *noOGGM* NEMO runs in the CAA region. Dots indicate differences that are not statistically significant, according to Wilcoxon signed-rank tests ($p > 0.05$). Colored land area indicates glacierized area as recorded in the RGI.

https://doi.org/10.5194/egusphere-2024-1425
Preprint. Discussion started: 18 June 2024

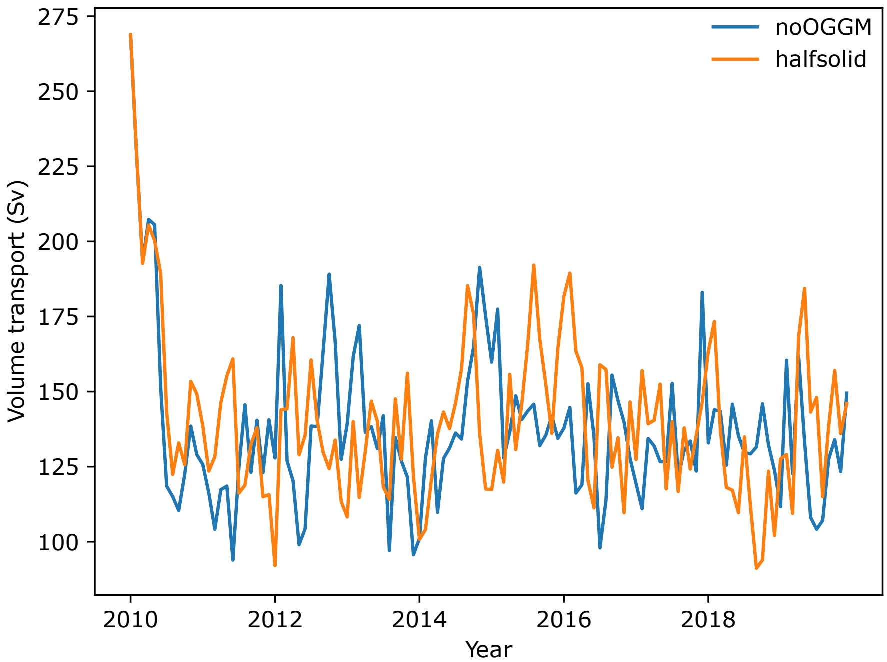

Figure A17. Positive (northward) transport across a section along 47°N (48.5°W to -11.5°W) in the *halfsolid* and the *noOGGM* NEMO runs. This transport feature mostly consists of the North Atlantic Current.

https://doi.org/10.5194/egusphere-2024-1425
Preprint. Discussion started: 18 June 2024

Author contributions. All three authors designed the study. JHM conceived and developed the changes to the glacier model code, prepared the data, conducted the numerical simulations and statistical evaluation, and wrote the manuscript. BM and PGM contributed to the manuscript.

Competing interests. The authors declare no competing interests.

Acknowledgements. This research has been supported by the Deutsche Forschungsgemeinschaft (DFG, grant no. IRTG 1904/3).

https://doi.org/10.5194/egusphere-2024-1425
Preprint. Discussion started: 18 June 2024

References

Alvarez-Solas, J., Robinson, A., Montoya, M., and Ritz, C.: Iceberg discharges of the last glacial period driven by oceanic circulation changes, Proceedings of the National Academy of Sciences, 110, 16 350–16 354, https://doi.org/https://doi.org/10.1073/pnas.1306622110, 2013.

Athanase, M., Provost, C., Artana, C., Pérez-Hernández, M. D., Sennéchael, N., Bertosio, C., Garric, G., Lellouche, J.-M., and Prandi, P.: Changes in Atlantic Water Circulation Patterns and Volume Transports North of Svalbard Over the Last 12 Years (2008–2020), Journal of Geophysical Research: Oceans, 126, e2020JC016 825, https://doi.org/https://doi.org/10.1029/2020JC016825, e2020JC016825 2020JC016825, 2021.

Bamber, J. L., Tedstone, A. J., King, M. D., Howat, I. M., Enderlin, E. M., van den Broeke, M. R., and Noel, B.: Land Ice Freshwater Budget of the Arctic and North Atlantic Oceans: 1. Data, Methods, and Results, Journal of Geophysical Research: Oceans, 123, 1827–1837, https://doi.org/https://doi.org/10.1002/2017JC013605, 2018.

Bartholomaus, T. C., Stearns, L. A., Sutherland, D. A., Shroyer, E. L., Nash, J. D., Walker, R. T., Catania, G., Felikson, D., Carroll, D., Fried, M. J., and et al.: Contrasts in the response of adjacent fjords and glaciers to ice-sheet surface melt in West Greenland, Annals of Glaciology, 57, 25–38, https://doi.org/10.1017/aog.2016.19, 2016.

Böning, C. W., Behrens, E., Biastoch, A., Getzlaff, K., and Bamber, J. L.: Emerging impact of Greenland meltwater on deepwater formation in the North Atlantic Ocean, Nature Geoscience, 9, 523–527, https://doi.org/10.1038/ngeo2740, 2016.

Born, A., Stocker, T. F., and Sandø, A. B.: Transport of salt and freshwater in the Atlantic Subpolar Gyre, Ocean Dynamics, 66, 1051–1064, https://doi.org/10.1007/s10236-016-0970-y, 2016.

Bouillon, S., Ángel Morales Maqueda, M., Legat, V., and Fichefet, T.: An elastic–viscous–plastic sea ice model formulated on Arakawa B and C grids, Ocean Modelling, 27, 174–184, https://doi.org/https://doi.org/10.1016/j.ocemod.2009.01.004, 2009.

Broecker, W. S.: Thermohaline Circulation, the Achilles Heel of Our Climate System: Will Man-Made CO_2 Upset the Current Balance?, Science, 278, 1582–1588, https://doi.org/10.1126/science.278.5343.1582, 1997.

Brunnabend, S.-E., Schröter, J., Timmermann, R., Rietbroek, R., and Kusche, J.: Modeled steric and mass-driven sea level change caused by Greenland Ice Sheet melting, Journal of Geodynamics, 59-60, 219–225, https://doi.org/https://doi.org/10.1016/j.jog.2011.06.001, mass Transport and Mass Distribution in the System Earth, 2012.

Caesar, L., McCarthy, G. D., Thornalley, D. J. R., Cahill, N., and Rahmstorf, S.: Current Atlantic Meridional Overturning Circulation weakest in last millennium, Nature Geoscience, 14, 118–120, https://doi.org/10.1038/s41561-021-00699-z, 2021.

Castro de la Guardia, L., Hu, X., and Myers, P. G.: Potential positive feedback between Greenland Ice Sheet melt and Baffin Bay heat content on the west Greenland shelf, Geophysical Research Letters, 42, 4922–4930, https://doi.org/https://doi.org/10.1002/2015GL064626, 2015.

Chafik, L., Holliday, N. P., Bacon, S., and Rossby, T.: Irminger Sea Is the Center of Action for Subpolar AMOC Variability, Geophysical Research Letters, 49, e2022GL099 133, https://doi.org/https://doi.org/10.1029/2022GL099133, e2022GL099133 2022GL099133, 2022.

Chatterjee, S., Raj, R. P., Bertino, L., Skagseth, O., Ravichandran, M., and Johannessen, O. M.: Role of Greenland Sea Gyre Circulation on Atlantic Water Temperature Variability in the Fram Strait, Geophysical Research Letters, 45, 8399–8406, https://doi.org/https://doi.org/10.1029/2018GL079174, 2018.

Cheng, L., Foster, G., Hausfather, Z., Trenberth, K. E., and Abraham, J.: Improved Quantification of the Rate of Ocean Warming, Journal of Climate, 35, 4827 – 4840, https://doi.org/https://doi.org/10.1175/JCLI-D-21-0895.1, 2022.

Dai, A., Qian, T., Trenberth, K. E., and Milliman, J. D.: Changes in continental freshwater discharge from 1948 to 2004, Journal of climate, 22, 2773–2792, https://doi.org/https://doi.org/10.1175/2008JCLI2592.1, 2009.

Davison, B. J., Cowton, T. R., Cottier, F. R., and Sole, A. J.: Iceberg melting substantially modifies oceanic heat flux towards a major Greenlandic tidewater glacier, Nature Communications, 11, 5983, https://doi.org/10.1038/s41467-020-19805-7, 2020.

Desbruyères, D., Chafik, L., and Maze, G.: A shift in the ocean circulation has warmed the subpolar North Atlantic Ocean since 2016, Communications Earth & Environment, 2, 48, https://doi.org/10.1038/s43247-021-00120-y, 2021.

Devilliers, M., Swingedouw, D., Mignot, J., Deshayes, J., Garric, G., and Ayache, M.: A realistic Greenland ice sheet and surrounding glaciers and ice caps melting in a coupled climate model, Climate Dynamics, 57, 2467–2489, https://doi.org/10.1007/s00382-021-05816-7, 2021.

Enderlin, E. M., Hamilton, G. S., Straneo, F., and Sutherland, D. A.: Iceberg meltwater fluxes dominate the freshwater budget in Greenland's iceberg-congested glacial fjords, Geophysical Research Letters, 43, 11,287–11,294, https://doi.org/https://doi.org/10.1002/2016GL070718, 2016.

Fofonoff, N. and Millard Jr, R.: Algorithms for the computation of fundamental properties of seawater, UNESCO Technical Papers in Marine Sciences, 44, https://doi.org/https://doi.org/10.25607/OBP-1450, 1983.

Foukal, N. P. and Lozier, M. S.: Assessing variability in the size and strength of the North Atlantic subpolar gyre, Journal of Geophysical Research: Oceans, 122, 6295–6308, https://doi.org/https://doi.org/10.1002/2017JC012798, 2017.

Frajka-Williams, E., Bamber, J. L., and Våge, K.: Greenland Melt and the Atlantic Meridional Overturning Circulation, Oceanography, 29, 22–33, https://doi.org/https://doi.org/10.5670/oceanog.2016.96., 2016.

Frederikse, T., Landerer, F., Caron, L., Adhikari, S., Parkes, D., Humphrey, V. W., Dangendorf, S., Hogarth, P., Zanna, L., Cheng, L., and Wu, Y.-H.: The causes of sea-level rise since 1900, Nature, 584, 393–397, https://doi.org/10.1038/s41586-020-2591-3, 2020.

Fu, Y., Li, F., Karstensen, J., and Wang, C.: A stable Atlantic Meridional Overturning Circulation in a changing North Atlantic Ocean since the 1990s, Science Advances, 6, eabc7836, https://doi.org/10.1126/sciadv.abc7836, 2020.

Garcia-Quintana, Y., Courtois, P., Hu, X., Pennelly, C., Kieke, D., and Myers, P. G.: Sensitivity of Labrador Sea Water Formation to Changes in Model Resolution, Atmospheric Forcing, and Freshwater Input, Journal of Geophysical Research: Oceans, 124, 2126–2152, https://doi.org/https://doi.org/10.1029/2018JC014459, 2019.

Giesen, R. H. and Oerlemans, J.: Calibration of a surface mass balance model for global-scale applications, The Cryosphere, 6, 1463–1481, https://doi.org/10.5194/tc-6-1463-2012, 2012.

Gillard, L. C., Pennelly, C., Johnson, H. L., and Myers, P. G.: The Effects of Atmospheric and Lateral Buoyancy Fluxes on Labrador Sea Mixed Layer Depth, Ocean Modelling, 171, 101 974, https://doi.org/https://doi.org/10.1016/j.ocemod.2022.101974, 2022.

Greene, C. H., Pershing, A. J., Cronin, T. M., and Ceci, N.: Arctic climate change and its impacts on the ecology of the North Atlantic, Ecology, 89, S24–S38, https://doi.org/https://doi.org/10.1890/07-0550.1, 2008.

Hakkinen, S. and Rhines, P. B.: Decline of subpolar North Atlantic circulation during the 1990s, Science, 304, 555–559, https://doi.org/https://doi.org/10.1126/science.1094917, 2004.

Harris, I., Osborn, T. J., Jones, P., and Lister, D.: Version 4 of the CRU TS monthly high-resolution gridded multivariate climate dataset, Scientific data, 7, 1–18, 2020.

Hattermann, T., Isachsen, P. E., von Appen, W.-J., Albretsen, J., and Sundfjord, A.: Eddy-driven recirculation of Atlantic Water in Fram Strait, Geophysical Research Letters, 43, 3406–3414, https://doi.org/https://doi.org/10.1002/2016GL068323, 2016.

Holland, P. R., Jenkins, A., and Holland, D. M.: The Response of Ice Shelf Basal Melting to Variations in Ocean Temperature, Journal of Climate, 21, 2558 – 2572, https://doi.org/https://doi.org/10.1175/2007JCLI1909.1, 2008.

Holliday, N. P., Bersch, M., Berx, B., Chafik, L., Cunningham, S., Florindo-López, C., Hátún, H., Johns, W., Josey, S. A., Larsen, K. M. H., Mulet, S., Oltmanns, M., Reverdin, G., Rossby, T., Thierry, V., Valdimarsson, H., and Yashayaev, I.: Ocean circulation causes the largest freshening event for 120 years in eastern subpolar North Atlantic, Nature Communications, 11, 585, https://doi.org/10.1038/s41467-020-14474-y, 2020.

Hu, A., Meehl, G. A., Han, W., and Yin, J.: Effect of the potential melting of the Greenland Ice Sheet on the Meridional Overturning Circulation and global climate in the future, Deep Sea Research Part II: Topical Studies in Oceanography, 58, 1914–1926, https://doi.org/https://doi.org/10.1016/j.dsr2.2010.10.069, climate and the Atlantic Meridional Overturning Circulation, 2011.

Hu, X. and Myers, P. G.: Changes to the Canadian Arctic Archipelago Sea Ice and Freshwater Fluxes in the Twenty-First Century under the Intergovernmental Panel on Climate Change A1B Climate Scenario, Atmosphere-Ocean, 52, 331–350, https://doi.org/10.1080/07055900.2014.942592, 2014.

Hugonnet, R., McNabb, R., Berthier, E., Menounos, B., Nuth, C., Girod, L., Farinotti, D., Huss, M., Dussaillant, I., Brun, F., et al.: Accelerated global glacier mass loss in the early twenty-first century, Nature, 592, 726–731, https://doi.org/https://doi.org/10.1038/s41586-021-03436-z, 2021.

Huss, M. and Hock, R.: Global-scale hydrological response to future glacier mass loss, Nature Climate Change, 8, 135–140, https://doi.org/10.1038/s41558-017-0049-x, 2018.

Hátún, H., Payne, M., Beaugrand, G., Reid, P., Sandø, A., Drange, H., Hansen, B., Jacobsen, J., and Bloch, D.: Large bio-geographical shifts in the north-eastern Atlantic Ocean: From the subpolar gyre, via plankton, to blue whiting and pilot whales, Progress in Oceanography, 80, 149–162, https://doi.org/https://doi.org/10.1016/j.pocean.2009.03.001, 2009.

Jackson, L. C., Biastoch, A., Buckley, M. W., Desbruyères, D. G., Frajka-Williams, E., Moat, B., and Robson, J.: The evolution of the North Atlantic Meridional Overturning Circulation since 1980, Nature Reviews Earth & Environment, 3, 241–254, https://doi.org/10.1038/s43017-022-00263-2, 2022.

Jenkins, A., Hellmer, H. H., and Holland, D. M.: The Role of Meltwater Advection in the Formulation of Conservative Boundary Conditions at an Ice–Ocean Interface, Journal of Physical Oceanography, 31, 285 – 296, https://doi.org/https://doi.org/10.1175/1520-0485(2001)031<0285:TROMAI>2.0.CO;2, 2001.

Kajanto, K., Straneo, F., and Nisancioglu, K.: Impact of icebergs on the seasonal submarine melt of Sermeq Kujalleq, The Cryosphere, 17, 371–390, https://doi.org/10.5194/tc-17-371-2023, 2023.

Kieke, D. and Yashayaev, I.: Studies of Labrador Sea Water formation and variability in the subpolar North Atlantic in the light of international partnership and collaboration, Progress in Oceanography, 132, 220–232, https://doi.org/https://doi.org/10.1016/j.pocean.2014.12.010, oceanography of the Arctic and North Atlantic Basins, 2015.

Kochtitzky, W., Copland, L., Van Wychen, W., Hugonnet, R., Hock, R., Dowdeswell, J. A., Benham, T., Strozzi, T., Glazovsky, A., Lavrentiev, I., Rounce, D. R., Millan, R., Cook, A., Dalton, A., Jiskoot, H., Cooley, J., Jania, J., and Navarro, F.: The unquantified mass loss of Northern Hemisphere marine-terminating glaciers from 2000–2020, Nature Communications, 13, 5835, https://doi.org/10.1038/s41467-022-33231-x, 2022.

Labe, Z., Magnusdottir, G., and Stern, H.: Variability of Arctic Sea Ice Thickness Using PIOMAS and the CESM Large Ensemble, Journal of Climate, 31, 3233 – 3247, https://doi.org/https://doi.org/10.1175/JCLI-D-17-0436.1, 2018.

Latif, M., Sun, J., Visbeck, M., and Hadi Bordbar, M.: Natural variability has dominated Atlantic Meridional Overturning Circulation since 1900, Nature Climate Change, 12, 455–460, https://doi.org/10.1038/s41558-022-01342-4, 2022.

Lavender, K. L., Davis, R. E., and Owens, W. B.: Mid-depth recirculation observed in the interior Labrador and Irminger seas by direct velocity measurements, Nature, 407, 66–69, https://doi.org/10.1038/35024048, 2000.

https://doi.org/10.5194/egusphere-2024-1425
Preprint. Discussion started: 18 June 2024

Lien, V. S., Vikebø, F. B., and Skagseth, Ø.: One mechanism contributing to co-variability of the Atlantic inflow branches to the Arctic, Nature Communications, 4, 1488, https://doi.org/10.1038/ncomms2505, 2013.

Liu, M. and Tanhua, T.: Water masses in the Atlantic Ocean: characteristics and distributions, Ocean Science, 17, 463–486, https://doi.org/10.5194/os-17-463-2021, 2021.

Lozier, M. S., Li, F., Bacon, S., Bahr, F., Bower, A. S., Cunningham, S. A., de Jong, M. F., de Steur, L., deYoung, B., Fischer, J., Gary, S. F., Greenan, B. J. W., Holliday, N. P., Houk, A., Houpert, L., Inall, M. E., Johns, W. E., Johnson, H. L., Johnson, C., Karstensen, J., Koman, G., Bras, I. A. L., Lin, X., Mackay, N., Marshall, D. P., Mercier, H., Oltmanns, M., Pickart, R. S., Ramsey, A. L., Rayner, D., Straneo, F., Thierry, V., Torres, D. J., Williams, R. G., Wilson, C., Yang, J., Yashayaev, I., and Zhao, J.: A sea change in our view of overturning in the subpolar North Atlantic, Science, 363, 516–521, https://doi.org/10.1126/science.aau6592, 2019.

Madec, G., Bourdallé-Badie, R., Bouttier, P.-A., Bricaud, C., Bruciaferri, D., Calvert, D., Chanut, J., Clementi, E., Coward, A., Delrosso, D., et al.: NEMO ocean engine, version 3.6 stable, Technical Report, Note du Pôle de modélisation de l'Institut Pierre-Simon Laplace 27, ISSN 1288-1619, 2016.

Malles, J.-H., Maussion, F., Ultee, L., Kochtitzky, W., Copland, L., and Marzeion, B.: Exploring the impact of a frontal ablation parameterization on projected 21st-century mass change for Northern Hemisphere glaciers, Journal of Glaciology, p. 1–16, https://doi.org/10.1017/jog.2023.19, 2023.

Marsh, R., Ivchenko, V. O., Skliris, N., Alderson, S., Bigg, G. R., Madec, G., Blaker, A. T., Aksenov, Y., Sinha, B., Coward, A. C., Le Sommer, J., Merino, N., and Zalesny, V. B.: NEMO–ICB (v1.0): interactive icebergs in the NEMO ocean model globally configured at eddy-permitting resolution, Geoscientific Model Development, 8, 1547–1562, https://doi.org/10.5194/gmd-8-1547-2015, 2015.

Marson, J. M., Myers, P. G., Hu, X., and Le Sommer, J.: Using Vertically Integrated Ocean Fields to Characterize Greenland Icebergs' Distribution and Lifetime, Geophysical Research Letters, 45, 4208–4217, https://doi.org/https://doi.org/10.1029/2018GL077676, 2018.

Marson, J. M., Gillard, L. C., and Myers, P. G.: Distinct Ocean Responses to Greenland's Liquid Runoff and Iceberg Melt, Journal of Geophysical Research: Oceans, 126, e2021JC017 542, https://doi.org/https://doi.org/10.1029/2021JC017542, e2021JC017542 2021JC017542, 2021.

Marzeion, B., Hock, R., Anderson, B., Bliss, A., Champollion, N., Fujita, K., Huss, M., Immerzeel, W. W., Kraaijenbrink, P., Malles, J.-H., et al.: Partitioning the uncertainty of ensemble projections of global glacier mass change, Earth's Future, 8, e2019EF001 470, 2020.

Masina, S., Storto, A., Ferry, N., Valdivieso, M., Haines, K., Balmaseda, M., Zuo, H., Drevillon, M., and Parent, L.: An ensemble of eddy-permitting global ocean reanalyses from the MyOcean project, Climate Dynamics, 49, 813–841, https://doi.org/10.1007/s00382-015-2728-5, 2017.

Maussion, F., Butenko, A., Champollion, N., Dusch, M., Eis, J., Fourteau, K., Gregor, P., Jarosch, A. H., Landmann, J., Oesterle, F., et al.: The open global glacier model (OGGM) v1. 1, Geoscientific Model Development, 12, 909–931, 2019.

McGeehan, T. and Maslowski, W.: Evaluation and control mechanisms of volume and freshwater export through the Canadian Arctic Archipelago in a high-resolution pan-Arctic ice-ocean model, Journal of Geophysical Research: Oceans, 117, https://doi.org/https://doi.org/10.1029/2011JC007261, 2012.

McKay, M. D., Beckman, R. J., and Conover, W. J.: A Comparison of Three Methods for Selecting Values of Input Variables in the Analysis of Output from a Computer Code, Technometrics, 21, 239–245, http://www.jstor.org/stable/1268522, 1979.

Moon, T., Sutherland, D. A., Carroll, D., Felikson, D., Kehrl, L., and Straneo, F.: Subsurface iceberg melt key to Greenland fjord freshwater budget, Nature Geoscience, 11, 49–54, https://doi.org/10.1038/s41561-017-0018-z, 2018.

https://doi.org/10.5194/egusphere-2024-1425
Preprint. Discussion started: 18 June 2024

Myers, P. G., Castro de la Guardia, L., Fu, C., Gillard, L. C., Grivault, N., Hu, X., Lee, C. M., Moore, G. W. K., Pennelly, C., Ribergaard, M. H., and Romanski, J.: Extreme High Greenland Blocking Index Leads to the Reversal of Davis and Nares Strait Net Transport Toward the Arctic Ocean, Geophysical Research Letters, 48, e2021GL094 178, https://doi.org/https://doi.org/10.1029/2021GL094178, e2021GL094178 2021GL094178, 2021.

Möller, M., Friedl, P., Palmer, S. J., and Marzeion, B.: Grounding Line Retreat and Ice Discharge Variability at Two Surging, Ice Shelf-Forming Basins of Flade Isblink Ice Cap, Northern Greenland, Journal of Geophysical Research: Earth Surface, 127, e2021JF006 302, https://doi.org/https://doi.org/10.1029/2021JF006302, e2021JF006302 2021JF006302, 2022.

Pennelly, C. and Myers, P. G.: Impact of Different Atmospheric Forcing Sets on Modeling Labrador Sea Water Production, Journal of Geophysical Research: Oceans, 126, e2020JC016 452, https://doi.org/https://doi.org/10.1029/2020JC016452, e2020JC016452 2020JC016452, 2021.

Pennelly, C. and Myers, P. G.: Tracking Irminger Rings' properties using a sub-mesoscale ocean model, Progress in Oceanography, 201, 102 735, https://doi.org/https://doi.org/10.1016/j.pocean.2021.102735, 2022.

Pfeffer, W. T., Arendt, A. A., Bliss, A., Bolch, T., Cogley, J. G., Gardner, A. S., Hagen, J.-O., Hock, R., Kaser, G., Kienholz, C., and et al.: The Randolph Glacier Inventory: a globally complete inventory of glaciers, Journal of Glaciology, 60, 537–552, https://doi.org/10.3189/2014JoG13J176, 2014.

Rainsley, E., Menviel, L., Fogwill, C. J., Turney, C. S. M., Hughes, A. L. C., and Rood, D. H.: Greenland ice mass loss during the Younger Dryas driven by Atlantic Meridional Overturning Circulation feedbacks, Scientific Reports, 8, 11 307, https://doi.org/10.1038/s41598-018-29226-8, 2018.

Raj, R. P., Chatterjee, S., Bertino, L., Turiel, A., and Portabella, M.: The Arctic Front and its variability in the Norwegian Sea, Ocean Science, 15, 1729–1744, https://doi.org/10.5194/os-15-1729-2019, 2019.

RGI Consortium: Randolph Glacier Inventory (RGI) - A Dataset of Global Glacier Outlines: Version 6.0, https://doi.org/10.7265/N5-RGI-60, 2017.

Rignot, E., Xu, Y., Menemenlis, D., Mouginot, J., Scheuchl, B., Li, X., Morlighem, M., Seroussi, H., den Broeke, M. v., Fenty, I., et al.: Modeling of ocean-induced ice melt rates of five west Greenland glaciers over the past two decades, Geophysical Research Letters, 43, 6374–6382, https://doi.org/https://doi.org/10.1002/2016GL068784, 2016.

Rudels, B., Björk, G., Nilsson, J., Winsor, P., Lake, I., and Nohr, C.: The interaction between waters from the Arctic Ocean and the Nordic Seas north of Fram Strait and along the East Greenland Current: results from the Arctic Ocean-02 Oden expedition, Journal of Marine Systems, 55, 1–30, https://doi.org/https://doi.org/10.1016/j.jmarsys.2004.06.008, 2005.

Sanchez, R., Slater, D., and Straneo, F.: Delayed Freshwater Export from a Greenland tidewater glacial fjord, Journal of Physical Oceanography, https://doi.org/https://doi.org/10.1175/JPO-D-22-0137.1, 2023.

Sévellec, F., Fedorov, A. V., and Liu, W.: Arctic sea-ice decline weakens the Atlantic Meridional Overturning Circulation, Nature Climate Change, 7, 604–610, https://doi.org/10.1038/nclimate3353, 2017.

Slater, D. A., Goldberg, D. N., Nienow, P. W., and Cowton, T. R.: Scalings for Submarine Melting at Tidewater Glaciers from Buoyant Plume Theory, Journal of Physical Oceanography, 46, 1839 – 1855, https://doi.org/https://doi.org/10.1175/JPO-D-15-0132.1, 2016.

Slater, T., Lawrence, I. R., Otosaka, I. N., Shepherd, A., Gourmelen, N., Jakob, L., Tepes, P., Gilbert, L., and Nienow, P.: Review article: Earth's ice imbalance, The Cryosphere, 15, 233–246, https://doi.org/10.5194/tc-15-233-2021, 2021.

Smith, G. C., Roy, F., Mann, P., Dupont, F., Brasnett, B., Lemieux, J.-F., Laroche, S., and Bélair, S.: A new atmospheric dataset for forcing ice–ocean models: Evaluation of reforecasts using the Canadian global deterministic prediction system, Quarterly Journal of the Royal Meteorological Society, 140, 881–894, https://doi.org/https://doi.org/10.1002/qj.2194, 2014.

Straneo, F. and Cenedese, C.: The Dynamics of Greenland's Glacial Fjords and Their Role in Climate, Annual Review of Marine Science, 7, 89–112, https://doi.org/10.1146/annurev-marine-010213-135133, pMID: 25149564, 2015.

Sun, J., Latif, M., and Park, W.: Subpolar Gyre–AMOC–Atmosphere Interactions on Multidecadal Timescales in a Version of the Kiel Climate Model, Journal of Climate, 34, 6583 – 6602, https://doi.org/https://doi.org/10.1175/JCLI-D-20-0725.1, 2021.

Timmermans, M.-L. and Marshall, J.: Understanding Arctic Ocean Circulation: A Review of Ocean Dynamics in a Changing Climate, Journal of Geophysical Research: Oceans, 125, e2018JC014 378, https://doi.org/https://doi.org/10.1029/2018JC014378, e2018JC014378 10.1029/2018JC014378, 2020.

von Schuckmann, K., Cheng, L., Palmer, M. D., Hansen, J., Tassone, C., Aich, V., Adusumilli, S., Beltrami, H., Boyer, T., Cuesta-Valero, F. J., Desbruyères, D., Domingues, C., García-García, A., Gentine, P., Gilson, J., Gorfer, M., Haimberger, L., Ishii, M., Johnson, G. C., Killick, R., King, B. A., Kirchengast, G., Kolodziejczyk, N., Lyman, J., Marzeion, B., Mayer, M., Monier, M., Monselesan, D. P., Purkey, S., Roemmich, D., Schweiger, A., Seneviratne, S. I., Shepherd, A., Slater, D. A., Steiner, A. K., Straneo, F., Timmermans, M.-L., and Wijffels, S. E.: Heat stored in the Earth system: where does the energy go?, Earth System Science Data, 12, 2013–2041, https://doi.org/10.5194/essd-12-2013-2020, 2020.

Wang, Q., Wekerle, C., Wang, X., Danilov, S., Koldunov, N., Sein, D., Sidorenko, D., von Appen, W.-J., and Jung, T.: Intensification of the Atlantic Water Supply to the Arctic Ocean Through Fram Strait Induced by Arctic Sea Ice Decline, Geophysical Research Letters, 47, e2019GL086 682, https://doi.org/https://doi.org/10.1029/2019GL086682, e2019GL086682 10.1029/2019GL086682, 2020.

Wassmann, P., Duarte, C. M., Agusti, S., and Sejr, M. K.: Footprints of climate change in the Arctic marine ecosystem, Global Change Biology, 17, 1235–1249, https://doi.org/https://doi.org/10.1111/j.1365-2486.2010.02311.x, 2011.

Weijer, W., Maltrud, M. E., Hecht, M. W., Dijkstra, H. A., and Kliphuis, M. A.: Response of the Atlantic Ocean circulation to Greenland Ice Sheet melting in a strongly-eddying ocean model, Geophysical Research Letters, 39, https://doi.org/https://doi.org/10.1029/2012GL051611, 2012.

Werder, M. A., Huss, M., Paul, F., Dehecq, A., and Farinotti, D.: A Bayesian ice thickness estimation model for large-scale applications, Journal of Glaciology, 66, 137–152, 2020.

Wood, M., Rignot, E., Fenty, I., Menemenlis, D., Millan, R., Morlighem, M., Mouginot, J., and Seroussi, H.: Ocean-Induced Melt Triggers Glacier Retreat in Northwest Greenland, Geophysical Research Letters, 45, 8334–8342, https://doi.org/https://doi.org/10.1029/2018GL078024, 2018.

Wood, M., Rignot, E., Fenty, I., An, L., Bjørk, A., van den Broeke, M., Cai, C., Kane, E., Menemenlis, D., Millan, R., Morlighem, M., Mouginot, J., Noël, B., Scheuchl, B., Velicogna, I., Willis, J. K., and Zhang, H.: Ocean forcing drives glacier retreat in Greenland, Science Advances, 7, eaba7282, https://doi.org/10.1126/sciadv.aba7282, 2021.

Xu, Y., Rignot, E., Fenty, I., Menemenlis, D., and Flexas, M. M.: Subaqueous melting of Store Glacier, west Greenland from three-dimensional, high-resolution numerical modeling and ocean observations, Geophysical Research Letters, 40, 4648–4653, https://doi.org/https://doi.org/10.1002/grl.50825, 2013.

Yeager, S., Castruccio, F., Chang, P., Danabasoglu, G., Maroon, E., Small, J., Wang, H., Wu, L., and Zhang, S.: An outsized role for the Labrador Sea in the multidecadal variability of the Atlantic overturning circulation, Science Advances, 7, eabh3592, https://doi.org/10.1126/sciadv.abh3592, 2021.

https://doi.org/10.5194/egusphere-2024-1425
Preprint. Discussion started: 18 June 2024

Zekollari, H., Huss, M., Farinotti, D., and Lhermitte, S.: Ice-Dynamical Glacier Evolution Modeling—A Review, Reviews of Geophysics, 60, e2021RG000 754, https://doi.org/https://doi.org/10.1029/2021RG000754, e2021RG000754 2021RG000754, 2022.

Zemp, M., Huss, M., Thibert, E., Eckert, N., McNabb, R., Huber, J., Barandun, M., Machguth, H., Nussbaumer, S. U., Gärtner-Roer, I., et al.: Global glacier mass changes and their contributions to sea-level rise from 1961 to 2016, Nature, 568, 382–386, https://doi.org/https://doi.org/10.1038/s41586-019-1071-0, 2019.